MATHEMATICAL MODELING AND STATISTICAL ANALYSIS OF THE CORTICAL MICROVASCULATURE AND HEMODYNAMIC RESPONSE

A Dissertation

Presented to the Faculty of the Graduate School

of Cornell University

In Partial Fulfillment of the Requirements for the Degree of

Doctor of Philosophy

by

Nathan Raj Cornelius

January 2014

MATHEMATICAL MODELING AND STATISTICAL ANALYSIS OF THE CORTICAL MICROVASCULATURE AND HEMODYNAMIC RESPONSE

Nathan Raj Cornelius, Ph.D.

Cornell University 2014

Mathematical models can serve as useful tools to better understand physiology and biological phenomena. This work outlines several mathematical models and their connection with various types of cortical microvascular topology and blood flow data obtained with various imaging modalities. Three models are proposed. The first is a model based on electrical circuit ideas that describes the relationship between cortical neural activity and space-resolved and time-resolved blood flows in the ensuing hemodynamic response. The second model, also based on electrical circuits, seeks to predict blood flows in a network of blood vessels based on topological network data and experimental blood flow measurements taken on a subset of vessels in the network. Finally, random graph ideas are used to propose two related models to represent the cortical microvasculature topology. The first is a Poisson process approach in which a vessel network is modeled by randomly positioning nodes in a three-dimensional space and randomly placing an edge between pairs of nodes based on various hard and soft constraints. The second related model is based on a Gibbsian Markov Random Field approach in which a vessel network is created using a Hamiltonian that favors or penalizes certain network features according to physiologic observations of vessel network topology. A wide range of applications of these types of models are demonstrated.

BIOGRAPHICAL SKETCH

Nathan Cornelius was born to Raj and Leverne Cornelius in Los Altos, California where he grew up and went to high school. He has two siblings—an older sister, Amber, and a younger brother, Josh. He earned a B.S. in Electrical Engineering and a B.A. in Economics at UCLA in 2006. Following his undergraduate career he went to Cornell University for graduate school, earning his M.Eng degree in 2008 in Electrical and Computer Engineering. He continued his graduate career at Cornell University in the field of Biomedical Engineering, earning his Ph.D. in 2014.

ACKNOWLEDGEMENTS

I would like to thank my family, friends, and committee members for their unwavering support over the course of my graduate student career. In particular I would like to thank my thesis advisor Peter Doerschuk for his patience, ideas, and guidance. I would also like to thank Dr. Nozomi Nishimura and my committee, Drs. Chris Schaffer and Al Molnar, for their insights and encouragement, especially in the vast area of neuroscience. I would finally like to thank Sandia National Laboratories for providing the fellowship that supported this work.

TABLE OF CONTENTS

CHAPTER 1

INTRODUCTION

Blood flow in the cerebral cortex plays a crucial role in providing tissue with oxygen and other molecules required to maintain proper function of the cortex, as well as clearing metabolites created from neuronal and glial activity. The cerebral vasculature and its topology are therefore of key importance as they provide the platform through which blood flow is regulated. For over a century, a relationship called the hemodynamic response has been experimentally observed, in which blood flow increases in response neuronal activity in a localized region of cortex [1]. Despite the longstanding awareness of this phenomenon, details regarding the underlying mechanisms linking neuronal activity to increased blood flow remain unresolved.

Models of various levels of the hemodynamic response, as well as models of the physical topology of the cortical vasculature can be helpful in elucidating information about the cortex and its behavior. Mathematical models can also be of importance when experimental limitations restrict an investigator's ability to collect certain types of data on a particular subject. While perturbations to the experimental subject can be difficult or impossible, the parameters of a mathematical model can be easily manipulated to mimic a particular experiment. This work proposes a variety of such models with a variety of goals, given the unique problems that each model is constructed to address.

The remainder of this work is organized as follows. Chapters 2 and 3 propose a mathematical model with the goal of interpreting intrinsic optical spectroscopy imaging (OISI) data in which space- and time-varying cerebral blood flow, cerebral blood volume, and blood oxygenation levels are the output. The model is "end-to-end", meaning that several interacting model compartments are connected to form a complete picture of the hemodynamic response. Chapter 2 is concerned mainly with the organization of the vascular and metabolic components of the model. Chapter 3 discusses the layer of the model that simulates neuronal activity, referred to as the electrical layer. The model presented in these chapters is constructed to connect to OISI data, but using a similar framework the model could easily be extended to connect to other types of data such as blood oxygenation level dependent (BOLD) signals gathered using functional magnetic resonance imaging (fMRI).

Chapter 4 presents a model which interprets imaging data gathered using an entirely different modality from Chapters 2 and 3. Developments in two-photon scanning laser microscopy (2PSLM) have enabled researchers to image blood vessels on a micron scale up to 1mm into the cortex, as well as record blood flow information by tracking the speed of individual red blood cells in a vessel [2]. Practical experimental limitations, such as the duration of time under which a subject can remain anesthetized, result in network data where topologically is fully mapped out, but blood flow information is incomplete and only determined for a subset of vessels in the network. The model in Chapter 4 can be used to predict blood flows in every blood vessel in a network, given topology (vessel lengths, widths, and connectivity) as well available experimentally measured blood flows. The model borrows electrical

engineering principles, such as Kirchhoff's Current Law and Ohm's Law, to construct a set of linear equations whose least-squares solution is the output of the model.

Chapter 5 introduces ideas for modeling the vascular topology using two different approaches. The first approach is a spatial Poisson process approach that is based loosely on the Erdős-Rényi model [3] where the nodes of the network represent vessel bifurcations and the edges of the network represent vessels. The model is constructed by employing an algorithm that distributes network nodes in a three-dimensional space according to (1) a Poisson process to randomly determine the number of nodes in the network, then (2) a uniform distribution in three dimensions to assign each of the nodes a particular location in the coordinate space. A decision is then made for every pair of nodes (vessel bifurcations) whether to connect them with an edge (vessel) according a binary random variable. The binary random variable is weighted by placing constraints on the Euclidean distance between two nodes in a network (to prevent vessels from being physiologically unreasonable in length) and the angle with respect to the cortical surface between the two nodes (to reflect physiology by favoring vessels that are more parallel to the cortical surface). Ideas from the model are applied to 2PLSM data to predict cortical layer boundaries based on expectation maximization methods.

A second generative model is discussed in Chapter 5 based on Gibbsian-Markov Random Fields. Two or three-dimensional space is discretized and each discrete space element is assigned either a one, meaning a vessel is present at that location, or a 0, meaning a vessel is not present. The binary assignment is made

randomly based on a Hamiltonian that places constraints on the network such as favoring nodes with edge degree three.

Chapter 6 is the final chapter of the thesis in which concluding remarks are made and possible directions for future research are discussed.

REFERENCES

[1] C.S. Roy and C.S. Sherrington. On the regulation of the blood supply of the brain. J. Physiol. pages 11:85–108, 1890.

[2] Thom P. Santisakultarm, Nathan R Cornelius, Nozomi Nishimura, Andrew I. Schafer, Richard T. Silver, Peter C. Doerschuk, William L. Olbricht and Chris B. Schaffer. In vivo two-photon excited fluorescence microscopy reveals cardiac- and respiration-dependent pulsatile blood flow in cortical blood vessels in mice. Am. J. Physiol Heart Circ Physiol, 302:H1367-H1377, 20 Jan. 2012.

[3] Paul Erdős and Alfréd Rényi. On Random Graphs. Publ Math. pages 6:290-297, 1959

CHAPTER 2

A MODEL OF THE CORTICAL MICROVASCULATURE AND METABOLISM

2.1 Introduction

Despite extensive study, the mechanisms of the local control of cerebral blood flow and cerebral blood volume by neuronal activity are not completely resolved [1–6]. A mathematical model is described whose purpose is to relate cortical electrical activity to flows and volumes of cerebral oxygenated and deoxygenated hemoglobin. While parts of the model are completely specified, *e.g.*, by conservation laws, other parts have flexibility that can be used to describe alternative mechanisms. Therefore many different models can be constructed by these methods, analogous to the flexibility of the models of Ref. [7]. To provide a concrete connection to at least one class of experimental result, the basic model is augmented with an optical model that allows it to describe optical intrinsic signal imaging (OISI) [8], essentially space-resolved and time-resolved optical reflectance spectroscopy measurements on surgically exposed cortex. An alternative choice would be to connect with BOLD and functional magnetic resonance imaging (fMRI).

An important goal is to describe both cerebral blood flow and cerebral blood volume. Therefore, when described in terms of an electrical circuit analog, the model has both resistors and capacitors. A second goal is to describe behavior when the space resolution is 10μm x 10μm implying that blood that enters the microvasculature in one pixel might exit in a different pixel. A third goal is to have a model that incorporates

physical constraints. Therefore, Kirchhoff's current and voltage laws are obeyed throughout and Laplace's and Poiseuille's laws are used to describe flow through a vessel where the contractile state of the vessel is described by the Young's Modulus of the vessel wall which is controlled by other quantities in the model. A fourth goal is to model both oxygenated and deoxygenated hemoglobin, including the conversion of oxygenated to deoxygenated. This requires a generalization of the usual Kirchhoff's laws to the situation where two types of current (oxygenated and deoxygenated) flow in the circuit. The neurovascular interaction is not completely understood and a fifth goal is to provide a model that is sufficiently flexible such that different interactions can be included in the model. A sixth goal is that the model be sufficiently simple that the parameters in the model can be determined for individual subjects rather than for populations of subjects. A seventh goal is to demonstrate the presence or absence of an initial decrease in HbO2 in response to an excitation is not necessarily due to a different structure for the mathematical model but rather could be due to the choice of parameters in a mathematical model of fixed structure. An eighth goal is to connect the model, with a typical spatial scale of roughly 10μm, to the macroscopic world which is done by deriving Grubb's law (a macroscopic relationship between cerebral blood volume and flow derived from whole-body medical imaging) from the model. Grubb's law can be interpreted as specifying the effective exponent in Poiseuille's law.

Because the model is nonlinear, it describes total signals and not perturbations in signals superimposed on an unmodeled baseline signal. Therefore, especially when

modeling the neurovascular interaction, the focus is on feedback models (the "metabolic hypothesis" [8]) in order to achieve long term homeostasis.

Because the model is connected to an OISI measurement model, the model is a 2-D array of pixels. Generalization to a 3-D array of voxels, suitable for a 3-D measurement modality, would be relatively straightforward, although it would likely be desirable to modify the neuroscience contained in the model for the depth direction relative to the two lateral directions.

Because (1) spatial resolution is too coarse to show cells, (2) the OISI data [8] is two dimensional rather than three dimensional, and (3) the goal is a simple model that can be personalized, the emphasis is on continuum models rather than models constructed of interacting cellular submodels. While the models are continuum models, spatially discretized versions of the continuum models are emphasized where the discretization is pixel-by-pixel. In the mathematics of the models, the spatially discretized model is a set of ordinary differential equations for each pixel and, if the pixel size is allowed to approach zero, the set of ordinary differential equations becomes a set of partial differential equations which is what is typically meant by a continuum model.

The cortical vasculature has a complicated 3-D structure [10, Figures 1 and 3]. While such a network could possibly be modeled as some form of random network, such a choice would make it difficult to determine the parameters in the model for individual subjects. Therefore, in Section 2.2, very simple deterministic networks are used.

The model has four interacting components, electrical, metabolic, vascular, and optical. The components are interconnected as is shown in Figure 2.1. The focus of this chapter is on the metabolic and vascular components.

Models of the neurovascular system typically involve many components and different components are modeled by different investigators with different levels of physical fidelity. For instance, the network topology of Ref. [10] is based on x-ray synchrotron images of 2.8mm^3 volumes of rat cortex and networks of similar fidelity are probably also available via 2-photon laser scanning microscopy (2PLSM) [9,11]. The networks used in the numerical examples shown in Chapter 3 are much more idealized, but the circuit ideas could be used in much more complicated and realistic networks. Some investigations focus on flows use purely resistive models [10] while other models based on Balloons [12] and Windkessel [13] ideas combine resistors and capacitors. In addition, some models describe input-output phenomenological behavior [7,14-16] while others focus on individual vessels [10,17]. The model described in this chapter is focused on individual vessel segments and describes the segments with circuits including both resistance and capacitance. Some investigators include extensive biochemistry in their models [18]. While the biochemistry described in this chapter is limited to the conversion of HbO_2 to HbR, additional molecules that are transported by the entering blood and metabolized dependent on brain activity could be included (Section 3.3).

The remainder of the model is presented in the following fashion. The four components of the model are described in the order vascular (Section 2.2.) and metabolic (Section 2.3), and electrical and optical (Section 3.2). Comparisons with

two sets of experimental data are described in Section 3.3 and example calculations demonstrating the spatial features of the model are also described in Section 3.3. The model makes it possible to compute many quantities related to cerebral blood volume and cerebral blood flow. As an example of such a calculation, in Section 3.4 the model's predictions for Grubb's Law [19] relating cerebral blood volume and flow are presented. Finally, the next chapter concludes with a discussion (Section 3.5).

2.2 Model: Vascular Component

For the cortex visualized in each pixel, the model includes vascular connections to the arterial supply, venous return, and to the adjacent four pixels. Each connection is a tube that can contribute to blood volume in that pixel and to flow through that pixel. Two types of tubes are used in the model. The simpler type has a fixed volume and resistance to flow. The more complicated type has wall that is described as a linear isotropic elastic material with a Young's Modulus which is denoted by E. When pressure in the tube increases the tube expands in diameter so that the volume increases and the resistance to flow decreases. Alternatively, when E increases ("stiffer") the diameter decreases and the resistance to flow increases and when E decreases ("floppier") the diameter increases and the resistance to flow decreases. The vascular system is thought of as being controlled by controlling the value of E. In a rough way, this corresponds to controlling the tone of the smooth muscle in the wall of small vessels. While it is not fundamental to the model, the model described in this manuscript uses the simpler fixed type of tube to describe the larger arterial vessels that connect a pixel to the arterial supply and the more complicated variable modulus type of tube to describe the smaller vessels that connect

a pixel (1) to the larger supply vessels, (2) to the smaller vessels in adjacent pixels, and (3) to the vascular return.

A diagram of the vascular component including the placement of the two types of tubes is shown in Figure 2.2. This figure is a simplification since it is one-dimensional, *i.e.*, for any given pixel there is a pixel to the "left" and the "right" of the given pixel but there should also be a pixel "above" and "below" of the given pixel in order to create a two-dimensional image and the "above" and "below" pixels are not shown. In Figure 2.2, blocks labeled T_0 are the larger arterial vessels that connect the tissue in a pixel to the arterial supply. They have a fixed volume and resistance to flow. The blocks labeled T_a are the arterioles that connect larger vessels to capillaries and have elastic walls described by a Young's Modulus which is controlled by the metabolic component of the model. The control of the Young's Modulus models the control of tone in the smooth muscle cells of arterioles which modulate the resistance to flow and the volume of the arteriole. The blocks labeled T_l and T_v are the capillaries connecting small arterial vessels to the venous return either directly within one pixel or indirectly via an adjacent pixel. These vessels also have elastic walls described by a Young's modulus but the value of the Young's Modulus is fixed rather than controlled since these vessels have little smooth muscle. It is only in the tubes modeling capillaries, *i.e.*, tubes labeled T_l or T_v, that conversion of HbO_2 to HbR occurs. The network of Figure 2.2 could be generalized, as is shown in Figure 2.3, to allow longer range interactions. The analysis of such a network is similar to what is done in this chapter.

The goal is to transform Figure 2.2 into an electric circuit analog so that a complete set of equations relating events in all pixels can be easily determined. In the electrical circuit analogy, fluid flow is electrical current and fluid pressure is electrical voltage. In reality, each of the blocks in Figure 2.2 represents a complicated network of vessels. The model described in this chapter describes the network as a parallel connection of identical branches. If there are N parallel branches then, looking ahead to Section 2.2.1, the T_0 block has resistance R_s/N where R_a is the resistance of one branch and volume NQ_a where Q_a is the volume of one branch. To simplify notation, the factor of N is not included in any of the formulas in this chapter. Before describing similar relationships for the other blocks, the details of the other blocks must be described and therefore the relationships are postponed until the end of Section 2.2.1.

The number of parallel branches depends on the size of the pixels. If the pixels are small, then most capillaries will start in one pixel and end in a different pixel. Therefore, in this case, the number of parallel branches in the T_l ("l" for "lateral") block is much greater than the number of parallel branches in the T_v ("v" for "venous") block. The use of small pixels in this optical experiment is one of the important contrasts with the fMRI experiment which uses relatively larger voxels.

2.2.1 Tubes with variable Young's Modulus

The tube with variable modulus is simultaneously described from two different points of view. In the first point of view, the tube is in equilibrium with a constant pressure throughout and the radius of the elastic wall is determined by the pressure and Young's Modulus (denoted by E). Let the Young's Modulus be described as $E(t) = E_0 + \delta_E(t)$ where E_0 is the nominal Young's Modulus and $\delta_E(t)$ is the perturbation in

the Young's Modulus due to control. Let t_w be the thickness of the wall. Let a_0 be the nominal and a the actual radius of the tube. Let P be the pressure in the tube. Then, the cylindrical form of the Law of Laplace [20, p. 71] is

$$\frac{aP}{t_w} = (E_0 + \delta_E)\frac{a - a_0}{a_0} \tag{2.1}$$

(the units are P: [Pressure]=[Force/Area^2]; E_0 and δ_E: [Force/Area^2]; a, a_0, and t_w: [Length]). Solving this equation for a gives a as a function of P and δ_E (as well as the nominal values E_0 and a_0 which are suppressed in the notation), specifically,

$$a(P, \delta_E) = \frac{\mathrm{E}_0 + \delta_E}{\dfrac{\mathrm{E}_0 + \delta_E}{a_0} - \dfrac{P}{t_w}}. \tag{2.2}$$

Let l denote the length of the tube and Q denote the volume of the tube. Then standard geometry (the volume of a cylinder) implies that Q as a function of P and δ_E is

$$Q(P, \delta_E) = \pi[a(P, \delta_E)]^2 l \tag{2.3}$$

$$= \left[\frac{\mathrm{E}_0 + \delta_E}{\dfrac{\mathrm{E}_0 + \delta_E}{a_0} - \dfrac{P}{t_w}}\right]^2 l. \tag{2.4}$$

$Q(P, \delta_E)$ is the tube's contribution to the blood volume of the cortex imaged in this particular pixel. In the eventual electric circuit, changes in $Q(P, \delta_E)$ with time are the charging and discharging of a capacitor with time.

In the second point of view, the tube is in the steady state with a difference of pressure between its ends and a fixed radius of the elastic wall and the fluid undergoes laminar flow through the tube. Poiseuille's formula [12] states that the pressure drop

from one end of the tube to the other end is proportional to the volume flow through the tube. Arbitrarily label the ends of the tube by 1 and 2. Let V_1 and V_2 be the pressures at End 1 and End 2, respectively, of the tube and let I be the volume flow into End 1. (If $I < 0$ then the flow is, in fact, out of End 1.) Let η be the dynamic viscosity of the fluid. Then Poiseuille's formula [20, p. 94] is

$$P_1 - P = \frac{8\eta l I}{\pi[a(P, \delta_E)]^4}. \tag{2.5}$$

Since the difference of pressures (P_1 - P_2) is linearly related to the flow (I), it is natural to define a resistance which is denoted by $R(P, \delta_E)$ and defined by

$$R(P, \delta_E) = \frac{8\eta l I}{\pi[a(P, \delta_E)]^4} \tag{2.6}$$

$$= \frac{8\eta l}{\pi}\left[\frac{\frac{\mathrm{E}_0 + \delta_E}{a_0} - \frac{P}{t_w}}{\mathrm{E}_0 + \delta_E}\right]^4. \tag{2.7}$$

In the eventual electric circuit, $R(P, \delta_E)$ is a resistor. Note that the dependence of viscosity η on radius a (*e.g.*, Ref. [22,23]) could be included but is only included in Section 3.4. Except for Section 3.4, including this effect would complicate the time derivatives because a depends on time and, therefore, η would also depend on time.

The two points of view are incompatible because the equilibrium point of view has a constant pressure throughout the entire tube and no flow while the steady state point of view has a varying pressure along the tube and flow. To merge these two points of view requires further modeling as is described in the remainder of this paragraph. Continue to label the two ends of the tube by 1 and 2. It is assumed that

one half of the resistance occurs at End 1 of the tube and one half at End 2, that no volume is stored in the resistive parts of the tube, and that all of the volume is stored between the resistive parts in an infinitesimal length of tube which has no resistance and whatever pressure is implied by the flows through the resistive parts of the tube. With these assumptions, a tube with variable modulus is exactly equivalent to a fragment of an electric circuit which is shown in Figure 2.6.

It is important to note that the capacitor in Figure 2.6 does not have a capacitance value. Instead, it is labeled by the amount of charge (*i.e.*, fluid volume), denoted by $Q(P, \delta_E)$, that it stores. The reason for this is that the capacitor in this model stores charge at zero voltage (*i.e.*, pressure) which is not possible in the standard capacitor in which charge is proportional to voltage. Therefore, the form of Kirchhoff's Current Law (KCL) at the node labeled by P is Figure 2.6 is

$$\frac{P(t)-P_1(t)}{R(P(t),\delta_E(t))/2}+\frac{P(t)-P_2(t)}{R(P(t),\delta_E(t))/2}+\frac{dQ(P(t),\delta_E(t))}{dt}=0 \tag{2.8}$$

where

$$\frac{dQ(P(t),\delta_E(t))}{dt}=\frac{dQ}{dP}(P(t),\delta_E(t))\frac{dP}{dt}(t)+\frac{dQ}{d\delta_E}(P(t),\delta_E(t))\frac{d\delta_E}{dt}(t). \tag{2.9}$$

Eqs. 2.8 and 2.9 imply a differential equation for P(t) which depends on $P_1(t)$ and $P_2(t)$, specifically,

$$\begin{aligned}\frac{dP}{dt}(t)=&\left[\frac{dQ}{dP}(P(t),\delta_E(t))\right]^{-1}\left[\frac{dQ}{d\delta_E}(P(t),\delta_E(t))\frac{d\delta_E}{dt}(t)\right.\\&\left.+\frac{P(t)-P_1(t)}{R(P(t),\delta_E(t))/2}+\frac{P(t)-P_2(t)}{R(P(t),\delta_E(t))/2}\right]\end{aligned} \tag{2.10}$$

The T_v, T_a, and T_l blocks of Figure 2.2 represent complicated networks of capillaries and other small vessels. The model described in this chapter describes the network as a parallel connection of identical branches. If there are N parallel branches then the block contains N parallel instances of the circuit of Figure 2.6, *i.e.*, all N instances of the node with voltage (pressure) P_1 are one node and likewise for the node with voltage (pressure) P_2 and the ground node. Since all resistors and all capacitors are identical, including identical time variation, if the capacitors all start with the same charge (volume), which is what is assumed in this model, then the voltages (pressures) labeled P in all circuits are identical. Therefore, the parallel combination of N circuits is identical to the original circuit with new parameter values: $R(P, \delta_E)/(2N)$ and $NQ(P, \delta_E)$. To simplify notation, the factor of N is not included in any of the formulas.

2.2.2 Fixed Tubes

The fixed tubes have a fixed volume, denoted by Q_a, which is always full and a fixed resistance to flow. Therefore, they are analogous to an electrical resistor of fixed value, denoted by R_a. The fixed volume, or equivalently charge, Q_a is outside of the electrical circuit model and does not enter the calculations until Section 2.2.5.

2.2.3 Electrical circuit and the solution for all voltages (*i.e.*, pressures)

By combining the electrical circuit fragments for the two types of tubes (Figure 2.5-6 the electrical circuit corresponding to the diagram of Figure 2.2 can be drawn. The analogy between the mechanical flow system and the electrical circuit is not perfect. In particular, for the analogy to be correct it must be that the initial conditions and the inputs to the circuit are such that the capacitor voltages are always positive. Failure to achieve this is equivalent to moving negative volumes of fluid in the

mechanical flow system, which is nonphysical. While no theorem has been proven about this situation, it is anticipated that maintaining positive capacitor voltages will not be difficult because P_a, the arterial supply pressure, is high and approximately constant and the changes in Young's Modulus, *i.e.*, the functions $\delta_E(t)$, are small changes. Note that the fundamental mechanical ideas based on linear elastic materials are themselves only valid for small changes. Less problematic than negative capacitor values are incorrect directions of flow. The direction of flow through the resistor labeled $R^{(a)}$ and the two resistors labeled $R(P_{i,j}^{(a)}(t), \delta_{E_{i,j}}(t))/2$ should be toward the node labeled $P_{i,j}^{(0)}$. Possibly the flow through the two resistors labeled $R(P_{i,j}^{(v)}(t), \delta_{E_{i,j}}(t))/2$ should be toward the ground. On the other hand, the flow through the two resistors labeled $R(P_{i,j}^{(R)}(t), \delta_{E_{i,j}}(t))/2$ can be in either direction. The same ideas used to avoid negative capacitor voltages will be sufficient to avoid incorrect flow directions also although, at the cost of increased complexity, the directions can be constrained by adding diodes to the circuit. Note the importance of limiting the size of the changes in capacitance; since the charge on a capacitor cannot change instantaneously, a decrease in capacitance leads to an increase in voltage which, if too great, could cause flow in the reversed direction.

Using standard circuit techniques, a system of ordinary differential equations for $P_{i,j}^{(v)}(t)$, $P_{i,j}^{(R)}(t)$, $P_{i,j}^{(L)}(t)$, $P_{i,j}^{(U)}(t)$, $P_{i,j}^{(D)}(t)$, and $P_{i,j}^{(a)}(t)$ can be derived. Then the solution for $P_{i,j}^{(0)}(t)$ can be determined by computing a linear combination of the four differential equation solutions. Solution of this system, which requires the functions

$\delta_{E_{i,j}}(t)$ as input (Section 2.3), determines all of the voltages (*i.e.*, pressures) in the image. From the voltages and the functions $\delta_{E_{i,j}}(t)$, all of the currents (*i.e.*, fluid flows) can be determined.

2.2.4 Flows are composed of two charge carriers (HbO_2 and HbR)

Two types of charge flow in the electric circuit created by combining Figures 2.2 and 2.5-6, specifically, HbO_2 and HbR. Furthermore, HbO_2 is converted to HbR by metabolism. Depending on the neuroscience included in the metabolism component of the model, there may be additional charge carriers which could also be treated by the methods of this section.

The part of the circuit in Figure 2.2 that connects the venous return node with the arterial node has not yet been explicitly discussed. A simple choice is a voltage source which represents the right heart, lungs, and left heart and which both sets both the arterial pressure and the arterial oxygen saturation (*i.e.*, the fraction of Hb that is HbO_2). In addition, in order to simplify the circuit equations, N_aN_b diodes are inserted, one diode in series with each without-capacitor tube T_0 with the forward direction in the direction of the T_a tubes as is shown in Figure 2.4 which ensures that all currents entering node *A* have arterial oxygen saturation.

Returning to the tube description of Figure 2.2 (rather than continuing with the circuit description achieved by inserting Figure 2.5-6 into Figure 2.2), the key idea is that pressures and total flow (HbR plus HbO2) are determined by Kirchhoff's Laws and that additional principles, described in this section, determine what fraction of the total flow is HbO_2. The basic principle is that of well mixing which occurs in two situations. First, the ratio of HbR to HbO_2 that flows out of a node is the result of

instantaneous well mixing of the flows into that node. For example, if there are two flows into a node, one flow of 2 *l*/s with .9 of the flow being HbO_2 and the second flow of 3 *l*/s with .8 of the flow being HbO_2 then the flow out of the node has a fraction $(2 \bar{\gamma} .9 + 3 \bar{\gamma} .8)/(2 + 3)$ of HbO_2. This calculation takes advantage of the fact that the total flows are known since knowledge of the total flows determines which flows are *into* versus *out of* the node of interest. Second, well mixing occurs in tubes that contribute to total blood volume, *i.e.*, tubes that contain capacitors. Specifically, for every capacitor, the ratio of HbR to HbO_2 that flows out of the capacitor is the result of integrated well mixing of the flows into that capacitor. In addition to well mixing, the only additional principle that is required is a principle for the conversion of HbO_2 to HbR, which is assumed to occur only in capacitors corresponding to capillaries and, in such capacitors, is a function of the amount of HbO_2 present in the capacitor.

In order to present sample equations resulting from the principles of the previous paragraph, let $f_\alpha(t)$ be the fraction of the flow out of the αth node that is HbO_2, let $u(x)$ be the unit step function ($u(x)$=1 for $x \geq 0$ and = 0 for $x < 0$), and let $r(x)$ be the unit ramp function ($r(x) = xu(x)$). In order to avoid more complicated notation, assume that the network has only one path between any pair of nodes. Let the set T_α contain the names of the with-capacitor tubes connected to the αth node. Let the set T_α be the names of the nodes connected by a without-capacitor tube T_0 to the αth node. Instantaneous well mixing at the αth node is described by the equation

$$f_\alpha = \frac{\sum_{\alpha' \in T_\alpha} \frac{Q_{\alpha'}^{HbO_2}(t)}{Q_{\alpha'}(t)} + \sum_{\alpha' \in T_\alpha} f_{\alpha'} r(i_{\alpha',\alpha}(t))}{\sum_{\alpha' \in T_\alpha} r(i_{\alpha',\alpha}(t)) + \sum_{\alpha' \in T_\alpha} r(i_{\alpha',\alpha}(t))} \tag{2.11}$$

where, as defined previously, $Q_{\alpha'}(t)$ and $Q_{\alpha'}^{HbO_2}(t)$ are the amount of Hb and HbO_2 stored in the capacitor at the α'th node, respectively, and $i_{\alpha',\alpha}(t)$ is the flow from the α'th to the αth node. This is instantaneous well mixing because all quantities are measured at the same time t and there are no derivatives or integrals.

Suppose a with-capacitor tube (index α) is the only path between two nodes (indexes α' and α''). Then the amount of HbO_2 in the well-mixed compartment of the αth with-capacitor tube is described by the differential equation

$$\begin{aligned} &\frac{dQ_\alpha^{HbO_2}}{dt}(t) = u(i_{\alpha',\alpha}(t))\, f_{\alpha'}(t) i_{\alpha',\alpha}(t) + u(i_{\alpha'',\alpha}(t))\, f_{\alpha''}(t) i_{\alpha'',\alpha}(t) \\ &+ \left[1 - u(i_{\alpha',\alpha}(t))\right] \frac{Q_\alpha^{HbO_2}(t)}{Q_{\alpha'}(t)} i_{\alpha',\alpha}(t) + \left[1 - u(i_{\alpha'',\alpha}(t))\right] \frac{Q_\alpha^{HbO_2}(t)}{Q_{\alpha''}(t)} i_{\alpha'',\alpha}(t) \\ &- \nu G(Q_\alpha^{HbO_2}(t) / Q(t)) \end{aligned} \tag{2.12}$$

$$\begin{aligned} &= r(i_{\alpha',\alpha}(t))\, f_{\alpha'}(t) + r(i_{\alpha'',\alpha}(t))\, f_{\alpha''}(t) \\ &- \left[r(-i_{\alpha',\alpha}(t)) + r(-i_{\alpha'',\alpha}(t)\right] \frac{Q_\alpha^{HbO_2}(t)}{Q_{\alpha'}(t)} \\ &- \nu G(Q_\alpha^{HbO_2}(t) / Q_\alpha(t)) \end{aligned} \tag{2.13}$$

where the conversion from Eq. 2.12 to Eq. 2.13 depends on the result that $[1 - u(x)]x = -r(-x)$ and where the term $\nu G(Q_\alpha^{HbO_2}(t) / Q_\alpha^2(t))$ describes the conversion of HbO_2 to HbR in the αth well-mixed compartment where $c_\alpha^{HbO_2}(t) = Q_\alpha^{HbO_2}(t) / Q_\alpha(t)$ is the volume fraction of HbO_2. The conversion term has a constant with units, *i.e.*, ν (units [Volume]/[Time]), multiplying a function, *i.e.*, $G(Q_\alpha^{HbO_2}(t) / Q_\alpha(t))$, and the function G is described in Section 2.2.6. This is integrated well mixing because all quantities are

measured at the same time t but it is the derivative with respect to time of the amount of HbO_2 in the capacitor (*i.e.*, $dQ_\alpha^{HbO_2}(t)/dt$) rather than the amount of HbO_2 in the capacitor (*i.e.*, $Q_\alpha^{HbO_2}(t)$) that is determined. Finally, note that masses are proportional to volumes. In particular, in terms of the number of hemoglobin molecules per erythrocyte (n_{Hb}), the molecular weight of hemoglobin (w_{Hb}), the volume of an erythrocyte (v_{RBC}), and the hematocrit (f, $0 < f < 1$), the mass (denoted by μ) is related to the volume (denoted by Q) by $\mu = (Qf/v_{RBC})n_{Hb}w_{Hb} = Q\kappa_{Q\to\mu}$ which defines $\kappa_{Q\to\mu}$. Therefore the concentration of HbO_2 is $\kappa_{Q\to\mu}\, c_\alpha^{HbO_2}(t)$.

2.2.5 HbO_2 and HbR per pixel

The value of $Q_\alpha^{HbO_2}(t)$ determines $Q_\alpha^{HbR}(t)$ by

$$Q_\alpha^{HbR}(t) = Q_\alpha(t) - Q_\alpha^{HbO_2}(t) \tag{2.14}$$

When computing the volume of oxygenated, deoxygenated, or total hemoglobin at a pixel (i,j) (denoted by $Q_{i,j}^{HbR}(t)$, $Q_{i,j}^{HbO_2}(t)$, and $Q_{i,j}(t)$) rather than in the capacitor at node α (denoted by $Q_\alpha^{HbR}(t)$, $Q_\alpha^{HbO_2}(t)$, and $Q_\alpha(t)$), it is necessary to divide the volume in a tube that crosses pixel boundaries between the pixels. In the calculations reported here, the partitioning is in equal parts.

2.2.6 Conversion of HbO_2 to HbR

A simple description of the conversion of HbO_2 to HbR is used: HbO_2 is converted to HbR plus energy and, because the conversion is enzymatic, it has a limited maximum rate. The description assumes that substrate other than HbO_2 is available in excess. Let the volume fraction of HbO_2 in capacitor α at time t be

denoted by $c_{\alpha}^{HbO_2}(t)$. Let the volume fraction of HbO_2 such that the rate is one-half the maximum rate be denoted by $c_{*}^{HbO_2}$. Then the Michaelis-Menten rate [13, pp. 192–194] is proportional to the quantity

$$G\left(c_{\alpha}^{HbO_2}(t)\right) = \frac{c_{\alpha}^{HbO_2}(t)}{c_{*}^{HbO_2}(t) + c_{\alpha}^{HbO_2}(t)} \tag{2.15}$$

which is a pure number (*i.e.*, no units).

Potentially, the maximum rate, v (Eq. 2.12) and/or the volume fraction at the half maximal rate, $c_{*}^{HbO_2}$ (Eq. 2.15), might be controlled. In this model, v is controlled but $c_{*}^{HbO_2}$ is not controlled and the control law for v is described as a part of the metabolic component in Section 2.3.2.

2.3 Model: Metabolic Component

The metabolic component fits between the electrical and vascular components and is essentially a control law. (1) Because the components are nonlinear, the metabolic component is a model for total signals not perturbations in signals around some baseline signal. Therefore, the metabolic component's control law is responsible for homeostasis as well the response to fluctuations, which is the response that is most often measured in experiments. (2) The goal is to model optical measurements that are sensitive to HbO_2 and HbR and so oxygenation is an important focus. If desired, other molecules can be given similar focus. (3) Because it fits between two other components, the metabolic component is constrained in terms of its inputs and outputs which must match those of the other two components. The output of the electrical component is $S(\mathbf{x}, t)$ (Eq. 3.1) which is also the input to the metabolic component. In spite of the obvious dependence of the electrical activity in the electrical component

on sufficient oxygenation, an output from the metabolic component as an input to the electrical component has not been included. The vascular component has one input from the metabolic component which is the Young's Modulus of the vessel wall, denoted by $E(t) = E_0 + \delta_{E_{i,j}}(t)$, which therefore must be an output of the metabolic component. Due to the focus on oxygenation, the metabolic component has one input from the vascular component which is the amount of HbO_2 present in the pixel. Additional inputs from the vascular component could be included if desired.

2.3.1 A feedback controller for energy homeostasis

A coupling process based on the "metabolic hypothesis" [5,8,14], in particular, a feedback process to achieve energy homeostasis, is described in this section. As is described in Section 2.3.3, to achieve homeostasis of some other molecular mediator by feedback would involve the same type of mathematics. Specifically, at each pixel $[(i, j)]$ there is a time varying $[t]$ energy budget variable denoted by $e_{i,j}(t)$ (units [Energy]) and a target value denoted by by e_* (units [Energy]). The energy budget variable $e_{i,j}(t)$ is at the core of a feedback loop. (1) Suppose $e_{i,j}(t)$ decreases. (2) Then the Young's Modulus $E(t) = E_0 + \delta_{E_{i,j}}(t)$ in the vascular component decreases so that the vessel wall becomes more floppy and therefore the vessel dilates. (3) Vessel dilation brings additional blood to the pixel and therefore additional HbO2 which is converted into HbR in order to create energy thereby increasing $e_{i,j}(t)$. Optionally, the conversion process itself could also be made more efficient which would also increase $e_{i,j}(t)$.

The mathematics to implement this feedback loop has two key components which are equations for the time variation of $e_{i,j}(t)$ and $E(t) = E_0 + \delta_{E_{i,j}}(t)$. The equation for $e_{i,j}(t)$ is a first-order differential equation saying that the rate of change of $e_{i,j}(t)$ with respect to time is the difference between production and consumption. Specifically, the equation is

$$\frac{de_{i,j}}{dt}(t) = \delta^{\uparrow}_{e_{i,j}}(t) - \delta^{\downarrow}_{e_{i,j}}(t) \tag{2.16}$$

where $\delta^{\uparrow}_{e_{i,j}}(t)$ is production and $\delta^{\downarrow}_{e_{i,j}}(t)$ is consumption.

The production of energy is proportional to the total rate of conversion of HbO_2 to HbR plus energy. The conversion of HbO_2 to HbR is described by the term $\nu G\left(Q_{\alpha}^{HbO_2}(t)\right)$ of Eq. 2.12. The proportionality constant v, which is the maximal rate, describes conversion of HbO_2 to HbR which has different units and potentially a different efficiency than the conversion of HbO_2 to $e_{i,j}(t)$. Therefore, a different proportionality constant, which is denoted by ν'_b (units [Energy]/[Time]) and describes the efficiency of the conversion of HbO_2 (and other substrates which are assumed to be in excess) into energy is needed. Therefore, the production of energy based on the HbO_2 in one particular capillary capacitor (the HbO_2 in non-capillary capacitors is not available for energy production) is $\nu'_b G\left(Q_{\alpha}^{HbO_2}(t)\right)$ where $Q_{\alpha}^{HbO_2}(t)$ is the oxygenated hemoglobin present in the αth capacitor which is a capillary capacitor. In addition, as before, R, L, U, and D tubes have equal values for their pressures and volumes and the equal values are denoted by variables with l index. Therefore,

$$\delta^{\uparrow}_{e_{i,j}}(t) = \nu'_b \left[4G\left(Q_{i,j,l}^{HbO_2}(t)\right) + G\left(Q_{i,j,v}^{HbO_2}(t)\right)\right]. \tag{2.17}$$

The consumption of energy is proportional to the power dissipated in the corresponding pixel of the electrical component plus a term for basal metabolism denoted by $\delta^{\downarrow}_{e_{i,j},0}$. In order to quantify this dissipation let $p_{i,j}$(t) (units [Energy]/[Time]) denote the power which is defined by

$$p_{i,j}(t) = S(\mathbf{x},t)\Delta_x\Delta_y \tag{2.18}$$

where $S(\mathbf{x},t)$ is the output of the electrical layer (Eq. 3.1), Δ_x and Δ_y are the sampling intervals in the x and y directions, and $\mathbf{x}=(i\,\Delta_x, j\,\Delta_y)$. The consumption is

$$\delta^{\downarrow}_{e_{i,j}}(t) = \gamma p_{i,j}(t) + \delta^{\downarrow}_{e_{i,j},0} \tag{2.19}$$

where γ (pure number) describes the efficiency of the electrical component, that is, how many units of metabolic energy are consumed in order to dissipate one unit of energy in the electrical component. This completes the description of the equation for $e_{i,j}(t)$.

The second key equation in the feedback loop is the equation for Young's Modulus $E(t) = E_0 + \delta_{E_{i,j}}(t)$. Because the pressure (voltage) equations depend on the derivative of $\delta_{Ei,j}(t)$ with respect to time t (*e.g.* Eq. 2.10), it is essential that $\delta_{E_{i,j}}(t)$ be smooth. For that reason, it is assumed that $E(t)$ obeys a critically-damped second order differential equation. The driving term for the differential equation and the single time constant of the differential equation differ depending on whether the budget variable $e_{i,j}(t)$ is above or below its threshold. When above threshold, there is a time constant τ_c for constriction of vessels and the steady state value of the Young's Modulus is E_0. When below threshold there is a time constant τ_d for dilation and the steady state value of the Young's Modulus is αE_0. In mathematical form,

$$\tau_c^2 \frac{d^2 E_{i,j}}{dt^2} + 2\tau_c \frac{dE_{i,j}}{dt} + E_{i,j} = E_0 \text{ if } e_{i,j} \geq e_* \tag{2.20}$$

$$\tau_d^2 \frac{d^2 E_{i,j}}{dt^2} + 2\tau_d \frac{dE_{i,j}}{dt} + E_{i,j} = \alpha E_0 \text{ if } e_{i,j} \leq e_* . \tag{2.21}$$

Since $E(t) = E_0 + \delta_{E_{i,j}}(t)$ and E_0 is constant with respect to time, Eqs. 2.20 and 2.21 imply that

$$\tau_c^2 \frac{d^2 \delta_{E_{i,j}}}{dt^2} + 2\tau_c \frac{d\delta_{E_{i,j}}}{dt} + \delta_{E_{i,j}} = 0 \text{ if } e_{i,j} \geq e_* \tag{2.22}$$

$$\tau_d^2 \frac{d^2 \delta_{E_{i,j}}}{dt^2} + 2\tau_d \frac{d\delta_{E_{i,j}}}{dt} + \delta_{E_{i,j}} = (\alpha - 1)E_0 \text{ if } e_{i,j} \leq e_* . \tag{2.23}$$

The equations presented concern the case where a budget is either above (desirable) or below (undesirable) a threshold. However, it might be the case that it is desirable to keep the budget between two thresholds rather than above a single threshold. This can be done by generalizing Eqs. 2.22 and 2.23 to have three rather than two cases.

2.3.2 Control of v

A controller for the maximal rate of conversion of HbO_2 to HbR, *i.e.*, *v*, is described in this section. The ideas are essentially the same as those used in Section 2.3.1. However, for $E_{i,j}$ in Section 2.3.1, it is necessary to have a smooth derivative with respect to time so Eqs. 2.20 and 2.21 are second order differential equations. For *v*, it is not necessary to have a smooth derivative so first order differential equations are used:

$$\tau_\upsilon \frac{d\upsilon_{i,j}}{dt} + \upsilon_{i,j} = \upsilon_b \text{ if } e_{i,j} \geq e_* \tag{2.24}$$

$$\tau_{\upsilon} \frac{d\upsilon_{i,j}}{dt} + \upsilon_{i,j} = \beta \upsilon_b \text{ if } e_{i,j} \le e_* . \tag{2.25}$$

2.3.3 Non-energy feedback controllers

In order to describe the optical measurements, this model has a detailed description of HbO_2 and HbR and the description includes the idea of an energy budget which controls the conversion of HbO_2 to HbR. As described in section 2.3.1, the same energy budget can control the Young's Modulus which controls the vascular component. But that is not necessary. If feedback still exists, then there is some other molecule *X* and its metabolite *X'* which are delivered by the vascular system and a budget related to *X* denoted by $e_{i,j}^X(t)$ with a target value denoted by e_*^X . Then, depending on whether $e_{i,j}^X(t) \ge e_*^X$ or $e_{i,j}^X(t) \le e_*^X$, the metabolic component sets the new value of the perturbation $\delta_{Ei,j}(t)$ in the Young's Modulus. The methods of this model can be directly applied to this case. First in order to include *X* and *X'*, the approach for HbO_2 and HbR of Sections 2.2.4 and 2.2.6 is duplicated for *X* and *X'*. Second, the differential equation for the energy budget (Eq. 2.16) is duplicated for the *X* budget, specifically

$$\frac{de_{i,j}^X}{dt}(t) = \delta_{e_{i,j}^X}^{\uparrow}(t) - \delta_{e_{i,j}^X}^{\downarrow}(t) \tag{2.26}$$

where $\delta_{e_{i,j}^X}^{\uparrow}(t)$ is the increase in $e_{i,j}^X(t)$ due to the vascular system bringing new *X* to the (*i,j*)th pixel and $\delta_{e_{i,j}^X}^{\downarrow}(t)$ is the decrease in $e_{i,j}^X(t)$ due to the electrical activity described by the voltage $v_{i,j}^m(t)$. Third, the relationship between $e_{i,j}^X(t)$ and $\delta_{Ei,j}(t)$ must be defined and the ideas of Section 2.3.1 can be used unaltered. Therefore as

soon as X is decided upon and the decrease in the X budget due to electrical activity, *i.e.*, $\delta^{\downarrow}_{e^X_{i,j}}(t)$ is determined, the new model is determined. The difference between depletion of a desired quantity and a buildup of an undesired quantity is whether $\delta^{\downarrow}_{e^X_{i,j}}(t)$ is positive or negative and whether $e^X_{i,j}(t) \geq e^X_*$ causes a decrease in the Young's Modulus (leading to dilation) or increase in the Young's Modulus (leading to constriction).

If more than one budget contributes to the control of the Young's Modulus then the simplest situation is if the control law is a linear combination of effects from the different budgets. The linear combination could occur at the budget variables. Alternatively, the linear combination could occur after the budget variables are transformed into perturbations of $\delta_{Ei,j}(t)$ on the Young's Modulus. In the latter case each perturbation could be generalized using the ideas of section 2.3.1 with time constants unique to that perturbation. Finally, and most generally, the transformation from budgets to the total perturbation $\delta_{Ei,j}(t)$ on the Young's Modulus could be a general multiple-input signal-output linear dynamical system with the budgets as inputs.

2.3.4 Feedforward Ideas

A coupling process based on the "neurogenic hypothesis" [2,3,8], in particular, a feedforward process, is sketched in this section. The goal of the metabolism component is to transform the signal $S(\mathbf{x}, t)$ from the electrical component into the perturbation $\delta_{E_{i,j}}(t)$ of the Young's Modulus which controls the vascular component. A possible biological mechanism is that a glial cell in contact with both one or more

neuronal synaptic clefts and spatially-local vascular smooth muscle cell senses the frequency with which a neurotransmitter is in the synaptic clefts and adjusts the tone of the smooth muscle cells. The adjustments last for a finite period of time and the adjustments are larger for higher frequency neuronal activity. One approach is to base the transformation on time-averaged second moments of $S(\mathbf{x},t)$ and its temporal derivative, *i.e.*,

$$\rho_{i,j}^{(0)}(t) = \frac{1}{T}\int_{t-T}^{t} \left[S(x,t)\right]^2 d\tau \tag{2.27}$$

$$\rho_{i,j}^{(1)}(t) = \frac{1}{T}\int_{t-T}^{t} \left[\frac{S(x,t)}{dt}(\tau)\right]^2 d\tau\,. \tag{2.28}$$

These moments are related to Sobolev norms of $S(\mathbf{x}, t)$ which have proven useful in signal and image processing problems. In particular, if $\rho_{i,j}^{(0)}(t)$ is greater than a threshold, denoted by ρ_*, then the perturbation $\delta_{E_{i,j}}(t)$ has an amplitude that is a linear regression of $\rho_{i,j}^{(0)}(t)$ and $\rho_{i,j}^{(1)}(t)$:

$$\delta_{E_{i,j}}(t) = \left(\kappa_{-1} + \kappa_0 \rho_{i,j}^{(1)}(t) + \kappa_1 \rho_{i,j}^{(1)}(t)\right)\boldsymbol{u}\left(\rho_{i,j}^{(0)}(t) - \rho_*\right). \tag{2.29}$$

As is discussed in Section 2.3.1, the perturbations in Young's Modulus due to oxygen homeostasis, any desired non-oxygen feedback controller, and the feedforward controller could be combined in a variety of ways. The simplest way is through a linear combination, specifically

$$\delta_{E_{i,j}}(t) = \omega^{HbO_2}\delta_{E_{i,j}}^{HbO_2}(t) + \omega^{X}\delta_{E_{i,j}}^{X}(t) + \omega^{FF}\delta_{E_{i,j}}^{FF}(t) \tag{2.30}$$

where the ω variables are constant weights and FF stands for feedforward.

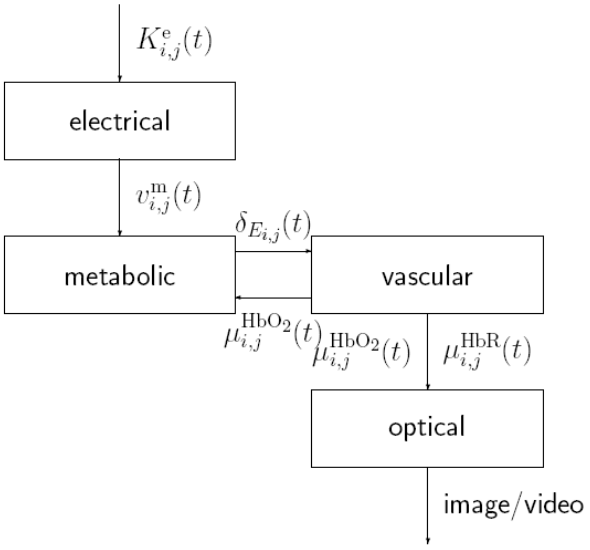

Figure 2.1: The four components of the model and their interactions shown as arrows which indicate the direction of the interaction.

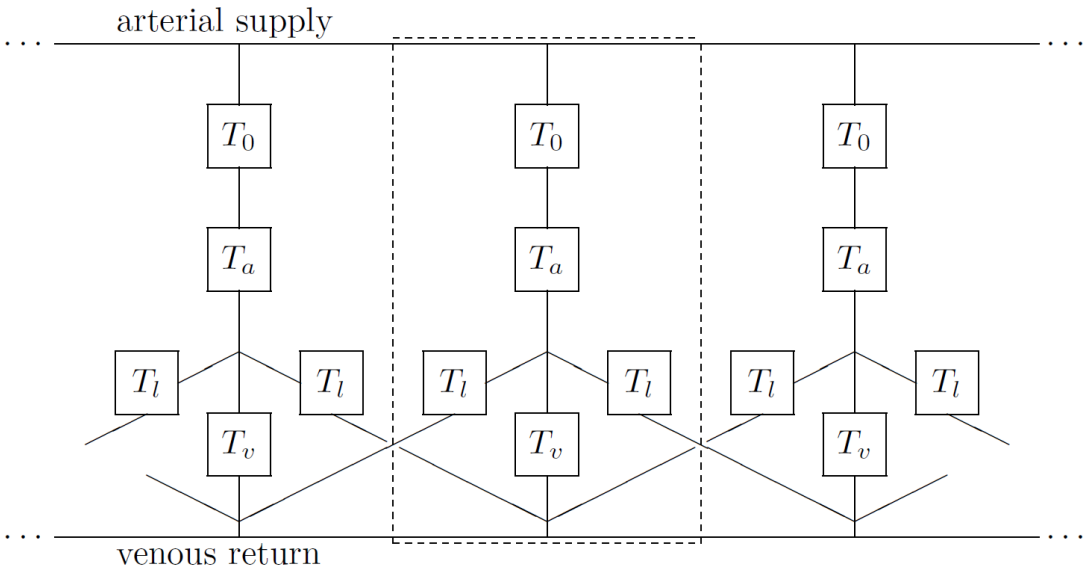

Figure 2.2: The simplest interconnection. The dashed lines enclose the part of the component which describes the cortex in a single pixel. Connections to pixels in front and behind are not shown for clarity. Half of the blood volume of each T_l block is attributed to each of the two pixels to which it is connected. Tubes labeled T_l and T_v model the capillary bed and so include conversion of HbO_2 to HbR while tubes labeled T_0 and T_a model pre-capillary vessels and so do not include the conversion.

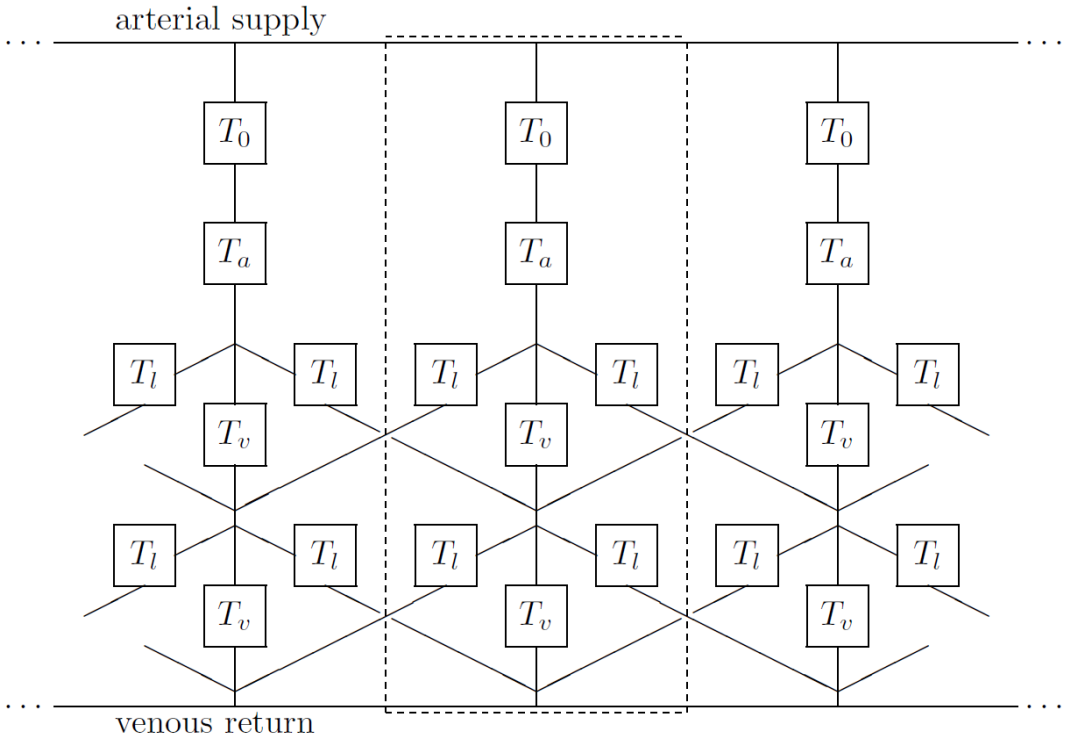

Figure 2:3: A more sophisticated interconnection allowing longer range interactions. The notation is identical to that of Figure 2.2. The duplication in each pixel of the triple of two T_l and one T_v block achieves the longer range interactions and additional duplications could be used to further increase the range.

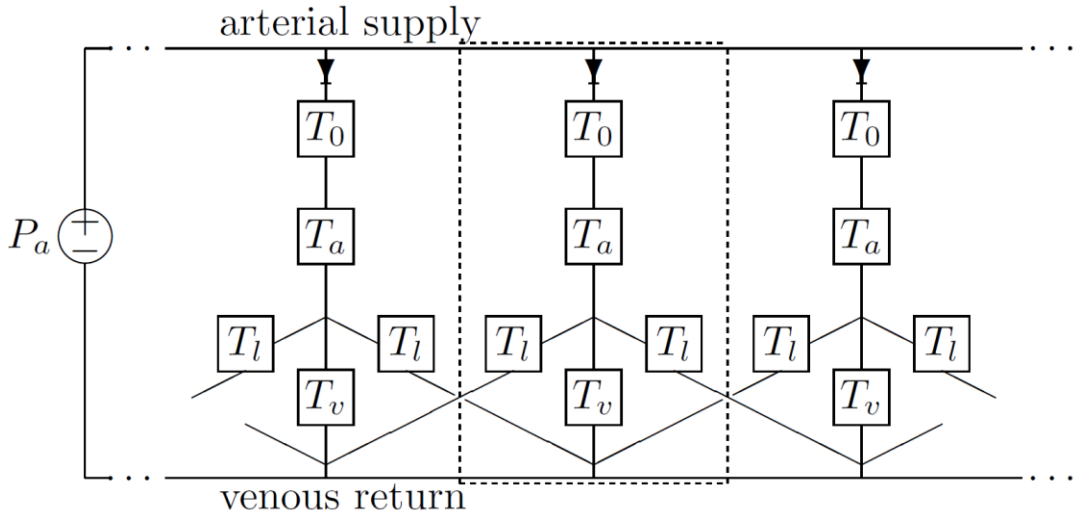

Figure 2.4: A complete version of Figure 2.2 which includes the sources and diodes to insure unidirectional flow.

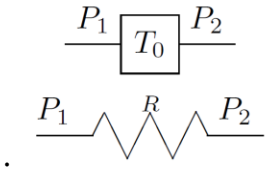

Figure 2.5: A purely resistive elementary component with fixed modulus (T_0) in block form as an electrical circuit.

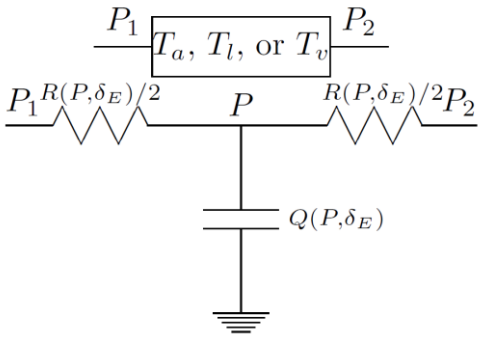

Figure 2.6: An elementary component with both resistive and capacitive characteristics and a variable modulus (T_a, T_l, or T_v) in block form as an electrical circuit. The resistor between P_1 and P (P_2 and P) in the electrical circuit might alternatively have the value $R(P_1, \delta_E)/2$ ($R(P_1, \delta_E)/2$).

REFERENCES

[1] David Kleinfeld, Pablo Blinder, Patrick J. Drew, Jonathan D. Driscoll, Arnaud Muller, Philbert S. Tsai, and Andy Y. Shih. A guide to delineate the logic of neurovascular signaling in the brain. Frontiers Neuroenergetics, 3(1), 25 Apr. 2011. doi:10.3389/fnene.2011.00001.

[2] David Attwell, Alastair M. Buchan, Serge Charpak, Martin Lauritzen, Brian A. MacVicar, and Eric A. Newman. Glial and neuronal control of brain blood flow. Nature, 468:232–243, 11 Nov. 2010.

[3] Bruno Cauli and Edith Hamel. Revisiting the role of neurons in neurovascular coupling. Frontiers Neuroenergetics, 2(9), 23 June 2010. doi:10.3389/fnene.2010.00009.

[4] Nicola B. Hamilton, David Attwell, and Catherine N. Hall. Pericyte-mediated regulation of capillary diameter: a component of neurovascular coupling in health and disease. Frontiers Neuroenergetics, 2(5), 21 May 2010. doi:10.3389/fnene.2010.00005.

[5] Olaf B. Paulson, Steen G. Hasselbalch, Egill Rostrup, GitteMoos Knudsen, and Dale Pelligrino. Cerebral blood flow response to functional activation. J. Cerebral Blood Flow & Metabolism, 30:2–14, 2010.

[6] Costantino Iadecola and Maiken Nedergaard. Glial regulation of the cerebral microvasculature. Nature Neuroscience, 10:1369–1376, 2007.

[7] Matthew J. P. Barrett, Merryn H. Tawhai, and Vinod Suresh. Arteries dominate volume changes during brief functional hyperemia: Evidence from mathematical modelling. NeuroImage, 62:482–492, 2012.

[8] Anna Devor, Sava Sakadzic, Vivek J. Srinivasan, Mohammad A. Yaseen, Krystal Nizar, Payam A. Saisan, Peifang Tian, Anders M. Dale, Sergei A. Vinogradov, Maria Angela Franceschini, and David A. Boas. Frontiers in optical imaging of cerebral blood flow and metabolism. J. Cerebral Blood Flow & Metabolism, pages 1–18, 18 Jan. 2012.

[9] Nozomi Nishimura, Nathanael L. Rosidi, Constantino Iadecola, and Chris B. Schaffer. Limitations of collateral flow after occlusion of a single cortical penetrating arteriole. J. Cerebral Bloof Flow & Metabolism, 30:1914–1927, 2010.

[10] Johannes Reichold, Marco Stampanoni, Anna Lena Keller, Alfred Buck, Patrick Jenny, and Bruno Weber. Vascular graph model to simulate the cerebral blood flow in realistic vascular networks. J. Cerebral Blood Flow and Metabolism, 29:1429–1443, 2009.

[11] Andy Y. Shih, Jonathan D. Driscoll, Patrick J. Drew, Nozomi Nishimura, Chris B. Schaffer, and David Kleinfeld. Two-photon microscopy as a tool to study blood flow and neurovascular coupling in the rodent brain. J. Cerebral Bloof Flow & Metabolism, 32:1–33, 2012.

[12] Richard B. Buxton, Eric C. Wong, and Lawrence R. Frank. Dynamics of blood flow and oxygenation changes during brain activation: The Balloon model. Magnetic Resonance in Medicine, 39:855–864, 1998.

[13] Joseph B. Mandeville, John J. A. Marota, C. Ayata, Greg Zaharchuk, Michael A. Moskowitz, Bruce R. Rosen, and Robert M. Weisskoff. Evidence of a cerebrovascular postarteriole Windkessel with delayed compliance. J. Cerebral Blood Flow and Metabolism, 19(6):679–689, 1999.

[14] Ying Zheng, Yi Pan, Sam Harris, Steve Billings, Daniel Coca, Jason Berwick, Myles Jones, Aneurin Kennerley, David Johnston, Chris Martin, Ian M. Devonshire, and John Mayhew. A dynamic model of neurovascular coupling: Implications for blood vessel dilation and constriction. NeuroImage, 52:1135–1147, 2010.

[15] Theodore J. Huppert, Monica S. Allen, Heval Benav, Phill B. Jones, and David A. Boas. A multicompartment vascular model for inferring baseline and functional changes in cerebral oxygen metabolism and arterial dilation. J. Cerebral Blood Flow and Metabolism, 27:1262–1279, 2007.

[16] Jinyuan Zhou, David A. Wilson, John A. Ulatowski, Richard J. Traystman, and Peter C. M. van Zijl. Two-compartment exchange model for perfusion quantification using aterial spin tagging. J. Cerebral Blood Flow and Metabolism, 21:440–455, 2001.

[17] David A. Boas, Stephanie R. Jones, Anna Devor, Theodore J. Huppert, and Anders M. Dale. A vascular anatomical network model of the spatio-temporal response to brain activation. NeuroImage, 40:1116–1129, 2008.

[18] Agnes Aubert and Robert Costalat. A model of the coupling between brain electrical activity, metabolism, and hemodynamics: Application to the interpretation of functional neuroimaging. NeuroImage, 52:1162–1181, 2002.

[19] Robert L. Grubb, Jr., Marcus E. Raichle, John O. Eichling, and Michel M. Ter Pogossian. The effects of changes in PaCO2 cerebral blood volume, blood flow, and vascular mean transit time. Stroke, 5:630–639, 1974.

[20] George A. Truskey, Fan Yuan, and David F. Katz. Transport Phenomena in Biological Systems. Pearson Prentice Hall, 2 edition, 2009. 23

[21] Edward W. Washburn. The dynamics of capillary flow. The Physical Review, 17(3):273–283, March 1921. Second series.

[22] A. R. Pries, T. W. Secomb, T. Gessner, M. B. Sperandio, J. F. Gross, and P. Gaehtgens. Resistance to blood flow in microvessels in vivo. Circulation Research, 75(5):904–915, November 1994.

[23] A. R. Pries and T. W. Secomb. Microvascular blood viscosity in vivo and the endothelial surface layer. Am. J. Physiol. Heart Circ. Physiol., 289:H2657–H2664, December 2005.

CHAPTER 3

A MODEL OF CORTICAL ELECTRICAL ACTIVITY AND ITS CONNECTION TO THE VASCULAR AND METABOLIC LAYERS

3.1 Introduction

In this chapter two different electrical layers are proposed which can connect to downstream metabolic and vascular components described in the previous chapter. The purpose of the electrical layer is to provide a framework which represents neural activity in the cortex. Because the spatial resolution of interest in the model is too large to resolve individual neuronal activity, the electrical layers presented are meant to represent a simplified and aggregated signal produced by many neurons. Experimentally, this electrical activity is commonly induced via direct stimulation by electrode or via indirect stimulation by inducing a sensory response (*e.g.*, whisker flicks or forepaw stimulation).

Numerical results, a mathematical relationship between this model and a previously described empirically observed relationship called Grubb's law, and a discussion are presented in the chapter's remaining sections.

3.2 An electrical layer

Cortex is an electrochemically active region of the body in which neurons produce electrical signals when induced to fire action potentials. In proper functioning cortex, electrical activity (energy expenditure) is met with a metabolic response in tissue in which ATP are created (energy replenishment) and used to restore ion

gradients. This section proposes two models of cortical electrical activity for the electrical layer. The first proposed layer is represented using a purely mathematical Sobolev norm-based framework which is usually nonlinear based on the parameter values chosen. The second proposed layer is based on a 2-dimensional linear circuit in which power and energy consumption can be directly computed as a function of the circuit's stimulus and resistances.

3.2.1 A Sobolev norm-based electrical layer

Suppose that there are multiple concurrent stimulations, in particular, let $s(\mathbf{x}, t)$ be the stimulation at position $\mathbf{x}$ and time t. The electrical component combines these stimulations to determine the total stimulation of the pixel at location $\mathbf{x}$ and time t (denoted by $S(\mathbf{x}, t)$) by including a special oscillation and decay factor z, a propagation speed c, and a potentially nonlinear superposition parameterized by the value of p according to the equation

$$S(\mathbf{x},t)=\begin{cases}\left[\int_{\mathbf{x}'\in\Re^2}\left|\mathrm{Re}\left\{\exp(z\|\mathbf{x}-\mathbf{x}'\|_2\right\}s(\mathbf{x}',t)\right|^p d^2\mathbf{x}'\right]^{1/p} & c=\infty \\ \left[\int_{\mathbf{x}'\in\Re^2}\left|\mathrm{Re}\left\{\exp(z\|\mathbf{x}-\mathbf{x}'\|_2\right\}s(\mathbf{x}',t-\|\mathbf{x}-\mathbf{x}'\|_2)/c)\right|^p d^2\mathbf{x}'\right]^{1/p} & \textit{otherwise}\end{cases} \tag{3.1}$$

where z is a complex constant, $\mathrm{Re}\{\cdot\}$ is the real part operation, and $\|\cdot\|_2$ is the Euclidian norm. If $z=1/\lambda$ and λ is real and negative then this equation represents exponential decay with space constant $-\lambda$. If $z=1/\lambda+\sqrt{-1}/\lambda'$ and λ is real and λ' is real and positive then this equation represents an oscillatory exponential decay with space constant $-\lambda$ for decay and period λ' for oscillation. Double stimulus experiments are considered in Section 3.3 in which case

$$s(\mathbf{x},t)=s_1(t)\delta(\mathbf{x}-\mathbf{x}_1)+s_2(t)\delta(\mathbf{x}-\mathbf{x}_2) \tag{3.2}$$

where $\delta(\cdot)$ is the Dirac delta-function in 2-D. In this case,

$$S(\mathbf{x},t)=\begin{cases}\left[\sum_{i\in\{1,2\}}\left|\mathrm{Re}\left\{\exp(z\|\mathbf{x}-\mathbf{x}'\|_2)s(\mathbf{x}',t)\right\}\right|^p\right]^{1/p} & c=\infty \\ \left[\sum_{i\in\{1,2\}}\left|\mathrm{Re}\left\{\exp(z\|\mathbf{x}-\mathbf{x}'\|_2)s(\mathbf{x}',t-\|\mathbf{x}-\mathbf{x}'\|_2)/c\right\}\right|^p\right]^{1/p} & \textit{otherwise}\end{cases} \tag{3.3}$$

In order to better understand the role of p, consider the case wehre the two stimuli are identical, z=0, and c=∞. Then,

$$S(\mathbf{x},t)=\left[2|s_1(t)|^p\right]^{1/p}=2^{1/p}|s_1(t)|. \tag{3.4}$$

For $\infty > p > 1$ the superposition is sublinear since $2^{1/p} < 2$, for p=1 the superposition is linear since $2^{1/1} = 2$, and for $1 > p > 0$ the superposition is supralinear since $2^{1/p} > 2$.

Many investigators report masses or concentrations of HbO_2 and HbR, which are the output of the vascular component of the model rather than the absorption spectra of light at each pixel. If, however, the absorption results are desired, the key tool is the Beer-Lambert Law which describes absorption of light. Since the cortical material is scattering, a portion of the light illuminating the cortex, after a path of length b through the cortex during which absorption occurs, is reradiated from the surface of the cortex and measured. This application of Beer-Lambert involves two types of scatterers, HbO_2 and HbR, and therefore two absorption cross sections σ^{HbO_2} and σ^{HbR}. Let I_0 be the incident radiation intensity and I be the re-radiated radiation intensity. The Beer-Lambert law for two types of scatterers is

$$I(\lambda)=I_0(\lambda)\exp(-\left[\sigma^{HbO_2}(\lambda)N^{HbO_2}+\sigma^{HbR}(\lambda)N^{HbR}\right]b(\lambda)) \tag{3.5}$$

where N^{HbO_2} and N^{HbR} are the number of particles of HbO_2 and HbR, respectively, present per unit volume in the volume through which the beam propagates and path length, both cross sections, and both intensities depend of the wavelength λ. In Section 2.3, μ^{HbO_2} and μ^{HbR} are defined to be the mass of HbO_2 and HbR, respectively, in a pixel and $\bar{\mu}^{HbO_2}$ and $\bar{\mu}^{HbR}$ are the corresponding values after incorporating the effect of the point spread function. Effectively add the missing third dimension of the model by assuming that the pixel has a third dimension Δ_z. Then

$N^{HbO_2} = \bar{\mu}^{HbO_2}/(w^{HbO_2}\Delta_x\Delta_y\Delta_z)$ and $N^{HbR} = \bar{\mu}^{Hbr}/(w^{HbR}\Delta_x\Delta_y\Delta_z)$ where $w^{HbO_2}(w^{HbR})$ converts $\bar{\mu}^{HbO_2}(\bar{\mu}^{HbR})$ with units of [Mass] to number of molecules which is dimensionless.

3.2.2 An Alternative Electrical Layer Using Linear Circuit Elements

At spatial scales greater than one neuron but still microscopic (*i.e.*, 10^{-3}–10^{-5}m), the paths of electrical excitation of the cortex are complicated. Perhaps models analogous to those developed for cardiac fibrillation could be used but such models describe phenomena at higher spatial resolution than can be seen in the optical data. Therefore, a simple model, a 2-D analog of the 1-D cable equation, can be used as an alternative model for the electrical layer already proposed in the previous section. While the motivation for the 2-D electrical circuit model are the same as for a 1-D cable model, the parameters of the 2-D model are not related to the 10^{-6}m spatial scale parameters used in a 1-D cable model to describe propagation of an action potential in an individual neuron. The circuit diagram depicting the electrical component is shown in Figure 3.1. As is described previously, this circuit is the 2-D

analog to the 1-D cable equation. A resistive planar outer cortical layer and a resistive planar inner cortical layer are connected by capacitive and conductive components. An electrical depolarization wave is generated at the current source K^e, and propagates radially outwards. Unlike the 1-D Hodgkin-Huxley cable model for axonal depolarization propagation and related models, there are no regenerative components in this proposed model. Hence the depolarization wave eventually dies away as it travels outwards from the source. The input to the electrical component is $K_{i,j}^{(e)}(t)$ and the output is $v_{i,j}^{(m)}(t)$ both for each pixel which is indexed by (i,j). The relationship between the input and output is determined in the remainder of this section.

Using KCL, Ohm's Law (*i.e.*, the *v*-*i* characteristics of a resistor), the *v*-*i* characteristics of a capacitor, and the definition

$$v_{i,j}^{(m)}(x,y,t) = v_{i,j}^{(in)}(x,y,t) - v_{i,j}^{(out)}(x,y,t) \tag{3.6}$$

a set of equations can be derived for $v_{i,j}^{(m)}(x,y,t)$ where the set of equations treats time t as a continuous variable but space (x,y) is discretized, where each set of r_{in}, r_{out}, C, and g_{m} in Figure 3.1 belong to a single pixel. Beginning with the KCL equations, the current traveling through the membrane, $K^m(x,y,t)\Delta_x\Delta_y$, is represented by a combination of four currents traveling form the four neighboring pixels to the pixel of interest on the inner layer. Likewise, the current exiting to the ground at a given pixel of interest is the excitation current, $K^e(x,y,t)\Delta_x\Delta_y$, minus the membrane current, $K^m(x,y,t)\Delta_x\Delta_y$, which equals a combination of the currents traveling along the outer layer from the neighboring pixels to the pixel of interest. The resulting equations are

$$K_{i,j}^{m}\Delta_x\Delta_y = \sum_{(i',j')\in N_{i,j}} i_{i',j'}^{in}\Delta \tag{3.7}$$

$$(K_{i,j}^{e} - K_{i,j}^{m})\Delta_x\Delta_y = \sum_{(i',j')\in N_{i,j}} i_{i',j'}^{out}\Delta \tag{3.8}$$

where the set of indices for the four neighbors of the (i,j)th pixel are denoted by $N_{i,j}$ = {(i+1,j), (i-1,j), (i,j+1), (i,j-1)} and Δ is defined by $\Delta = \Delta_x$ for $(i', j') \in \{(i, j+1), (i, j-1)\}$ and = Δ_y for $(i', j') \in \{(i+1, j), (i-1, j)\}$. Using Ohm's law, the relationships between currents, voltages, and resistances along the inner and outer layers can be expressed in the following pair of equations:

$$\sum_{(i',j')\in N_{i,j}} (v_{i',j'}^{in} - v_{i,j}^{in}) = r_{in} \sum_{(i',j')\in N_{i,j}} i_{i',j'}^{in}\Delta \tag{3.9}$$

$$\sum_{(i',j')\in N_{i,j}} (v_{i',j'}^{out} - v_{i,j}^{out}) = r_{out} \sum_{(i',j')\in N_{i,j}} i_{i',j'}^{out}\Delta . \tag{3.10}$$

Combining Eqs. 3.7 and 3.9 and Eqs. 3.8 and 3.10 provides relationships between inner and outer voltages and the membrane and excitation currents:

$$K_{i,j}^{m}\Delta_x\Delta_y = \frac{1}{r_{in}} \sum_{(i',j')\in N_{i,j}} (v_{i',j'}^{in} - v_{i,j}^{in}) \tag{3.11}$$

$$(K_{i,j}^{e} - K_{i,j}^{m})\Delta_x\Delta_y = \frac{1}{r_{out}} \sum_{(i',j')\in N_{i,j}} (v_{i',j'}^{out} - v_{i,j}^{out}) . \tag{3.12}$$

As described in Eq. 3.6, membrane voltage at the (i,j)th pixel, denoted by $v_{i,j}^{m}$, is the difference between the voltage of the inner layer and the voltage of the outer layer at that pixel, *i.e.*, $v_{i,j}^{in} - v_{i,j}^{out}$. Using the definition of v^m gives

$$\sum_{(i',j')\in N_{i,j}} (v_{i',j'}^{m} - v_{i,j}^{m}) = \sum_{(i',j')\in N_{i,j}} (v_{i',j'}^{in} - v_{i,j}^{in}) - \sum_{(i',j')\in N_{i,j}} (v_{i',j'}^{out} - v_{i,j}^{out}) . \tag{3.13}$$

From Eqs. 3.11 and 3.12 it follows that

$$\sum_{(i',j')\in N_{i,j}} (v_{i',j'}^{in} - v_{i,j}^{in}) = r_{in} K_{i,j}^{m} \Delta_x \Delta_y \tag{3.14}$$

$$\sum_{(i',j')\in N_{i,j}} (v_{i',j'}^{out} - v_{i,j}^{out}) = r_{out} (K_{i,j}^{e} - K_{i,j}^{m}) \Delta_x \Delta_y . \tag{3.15}$$

Substituting Eqs 3.14 and 3.15 into Eq. 3.13 gives a relationship strictly between membrane voltage and membrane current, excitation current, and inner and outer resistances:

$$\sum_{(i',j')\in N_{i,j}} (v_{i',j'}^{m} - v_{i,j}^{m}) = r_{in} K_{i,j}^{m} \Delta_x \Delta_y - r_{out} (K_{i,j}^{e} - K_{i,j}^{m}) \Delta_x \Delta_y \tag{3.16}$$

$$= K_{i,j}^{m} \Delta_x \Delta_y (r_{in} + r_{out}) - K_{i,j}^{e} \Delta_x \Delta_y r_{out}. \tag{3.17}$$

The membrane current at the (i,j)th pixel flows through a resistor and capacitor in parallel, so it can be expressed in terms of membrane conductance, g, and membrane capacitance, C. Since the current through the conductance $g\Delta_x\Delta_y v_{i,j}^{m}$ is and the current through the capacitance is $C\Delta_x\Delta_y \dfrac{dv_{i,j}^{m}}{dt}$, it follows from KCL that

$$K_{i,j}^{m} \Delta_x \Delta_y = g\Delta_x \Delta_y v_{i,j}^{m} + C\Delta_x \Delta_y \frac{dv_{i,j}^{m}}{dt} . \tag{3.18}$$

Combining Eqs. 3.17 and 3.18 gives

$$\sum_{(i',j')\in N_{i,j}} (v_{i',j'}^{m} - v_{i,j}^{m}) = \left(g v_{i,j}^{m} + C \frac{dv_{i,j}^{m}}{dt} \right) (r_{in} + r_{out}) \Delta_x \Delta_y - K_{i,j}^{e} \Delta_x \Delta_y r_{out} \tag{3.19}$$

which can be rearranged to the form

$$\frac{dv_{i,j}^{m}}{dt} = \frac{1}{(r_{in} + r_{out}) C \Delta_x \Delta_y} \sum_{(i',j')\in N_{i,j}} (v_{i',j'}^{m} - v_{i,j}^{m}) - \frac{g}{C} v_{i,j}^{m} + \frac{r_{out}}{(r_{in} + r_{out}) C} K_{i,j}^{e} . \tag{3.20}$$

Eq. 3.20 is a system of coupled ordinary differential equations, one equation for each pixel, for the membrane voltage as a function of the excitation $K_{i,j}^{e}$. In the limit as $\Delta_x \to 0$ and $\Delta_y \to 0$, this system becomes a partial differential equation in two space variables and time, which will be described in the following section. For the ease of software development that links this electrical layer to the vascular layer, it is advantageous to use the ordinary differential equations described for each discrete pixel rather than partial differential equations.

The reason the electrical layer proposed in the previous section, rather than the 2-D planar electrical circuit layer proposed in this section, is used to drive the vascular and metabolic layers is purely phenomenological. Electrode recordings of rodent cortex in response to whisker stimulation have shown to produce a "center-surround" response in which electrical activity in the cortical area corresponding to the flicked whisker increases, while activity in the surrounding regions is suppressed due to lateral inhibition [1]. This leads to qualitative behavior which the 2-D circuit discussed in this section cannot replicate. For example, because of the center-surround phenomenon observed experimentally, it has been shown that simultaneously stimulating multiple whiskers results in a sublinear electrical response compared to the response achieved by linearly superpositioning the activity produced by flicking whiskers individually. Because the circuit is purely linear with passive components (resistors and capacitors), it is impossible to achieve an electrical response that is anything other than purely additive when multiple sources of stimulation are present [2]. The electrical layer described in the previous section, however, is advantageous in that sublinear behavior can be attained with proper selection of the exponent *p*.

While the layer described in the previous section is better suited to achieve nonlinearity, it can be viewed as a less physical way of representing electrical activity in cortex. One of the attractive features of the 2-D planar circuit presented in this section is that energy dissipated in a pixel can be computed based on the current flowing through that pixel and the impedance values of the resistors within the pixel. Therefore a less abstract value for the energy that has been dissipated in a specific pixel can be input to the downstream metabolic and vascular layers.

3.2.3 The case of an impulsive excitation

In the limit as $\Delta_x \to 0$ and $\Delta_y \to 0$, Eq. (3.20) becomes the partial differential equation:

$$\nabla^2 v^m = \left[g v^m + C \frac{\partial v^m}{dt} \right] (r_{in} + r_{out}) - K^e(x,y,t) r_{out} . \tag{3.21}$$

Letting the excitation be 0, the PDE can be represented more simply in the form

$$a^2 \nabla^2 v^m = v^m + b \frac{\partial v^m}{\partial t} \tag{3.22}$$

which allows a separation of variables by assuming $v^m = X(x)Y(y)T(t)$ so that the PDE becomes

$$a^2 \frac{\partial^2 X}{\partial x^2} YT + a^2 \frac{\partial^2 Y}{\partial y^2} XT = XYT + b \frac{\partial T}{\partial t} XY . \tag{3.23}$$

Solving gives the general solution where

$$X = e^{-j\frac{p}{a}x}, \qquad Y = e^{-j\frac{q}{a}y}, \qquad T = e^{-\frac{1}{b}(q^2+p^2+1)t} \tag{3.24}$$

which is valid for any p and q. Therefore it is possible to linearly suppose all possibilities of p and q using a function $H(p,q)$ to get

$$v^m(x,y,t) = \int_{-\infty}^{\infty}\int_{-\infty}^{\infty} H(p,q)e^{-j\frac{p}{a}x} e^{-j\frac{q}{a}y} e^{-\frac{1}{b}(q^2+p^2+1)t} dqdp\,. \tag{3.25}$$

Setting t to 0 and rearranging gives.

$$v^m(x,y,0) = \int_{-\infty}^{\infty}\int_{-\infty}^{\infty} H(p,q)e^{-j(\frac{p}{a}x+\frac{q}{a}y)} dqdp \tag{3.26}$$

which is simply the 2-D Fourier transform of $H(p,q)$. If v^m at t=0 is impulsive, *i.e.*, $v^m(x,y,0)=\delta(x,y)$, then

$$v^m(x,y,t) = \frac{A}{t} e^{\frac{-(x^2+y^2)b}{4a^2t}} \tag{3.27}$$

where $A=b/(8\pi^2)$, $b=c/g$, and $a^2=1/(g(r_{in}+r_{out}))$. Therefore v^m takes the form related to a circularly symmetric 2-D Gaussian distribution which has variance that increases as time t increases. The function broadens spatially and shrinks in amplitude as time goes on.

3.3 Numerical Results

Much OISI data is published in terms of the time-course of hemoglobin concentrations, often at a single location. Therefore, no optics is included in the model. In addition, when only a single location is considered, the model is further simplified to a model of a single pixel which implies that no electrical layer is included. The predictions of the mathematical model are computed by a program written in the Matlab programming language [5].

The stimulus in Ref. [9] is forepaw stimulation of the rat while the stimulus in Ref. [10] is stimulation of the whisker pad of the rat. In both cases, the resulting signal in the cortex is not known. For this reason, some of the signals in the model have an arbitrary energy unit. This unit eventually cancels out when computing quantities of

interest such as μ^{HbT}. In the metabolic component of the model, signed energy terms are used so that e_*, the target value for the energy budget (See Section 2.3.1, Eqs. 2.20 and 2.21) can be taken to be zero which needs no unit. Also in the metabolic component of the model, the Michaelis-Menten conversion of HbO_2 to HbR and energy has the same arbitrary unit for the energy.

Although it is not fundamental to the modeling approach, in this model it is assumed that the hematocrit is constant. Therefore in some standard volume, the sum of the masses of oxygenated and deoxygenated hemoglobin ($\mu^{HbO_2} + \mu^{HbR}$) is constant; the sum of the concentrations ($c^{HbO_2} + c^{HbR}$) is constant; and, since hemoglobin only occurs in the two forms, the sum of the fractions ($f^{HbO_2} + f^{HbR}$) is one. Because fractions are restricted to the interval from 0 to 1, which is not true for concentrations or masses, the computer program generally uses fractions.

Figure 3.3 shows the response of the model using the nominal parameters. The parameters chosen result in a moderate initial dip in the concentration of HbO_2 in these noise-free curves.

Figures 3.8 and 3.9 show how key responses of the model change as a function of changes in six of the parameters in the model. The responses that are displayed are (1) concentration of oxygenated hemoglobin ($Q^{\mathrm{HbO2}}(t)/Q^{\mathrm{HbT}}(t)$), (2) concentration of deoxygenated hemoglobin ($Q^{\mathrm{HbR}}(t)/Q^{\mathrm{HbT}}(t)$), (3) total mass of hemoglobin ($\mu^{\mathrm{HbT}}(t)$), and (4) cerebral blood flow (CBF). By changes in parameters only, a wide range of amplitude changes occur, including changes in the amplitude of the initial dip in the

concentration of HbO2. Changes in duration are much more moderate, because the input is the same for all 30 choices of parameter values.

Figure 3.4 shows the hemoglobin curves for an example modeled on Ref. [9, Figure 3] which describes the response in a rat to forepaw stimulation at 3Hz for 10s. This is a longer duration stimulation than the 2s duration of the stimulation in Figures 3.3, 3.5–3.9 and therefore the duration of the response is longer. More interestingly, and similar to the experimental data in Ref. [9, Figure 3], the decay from the peak signals is in two phases with an intermediate plateau. The initial peak in HbO_2 is due to the presence of the temporal derivative of the Young's modulus, *i.e.*, $d\delta_E/dt$, in Eq. 2.10.

Figure 3.5 shows hemoglobin and cerebral blood flow curves for an example modeled on Ref. [10, "Awake" panels of Figure 6, p. 39]. While the example in Figure 3.4 considered an input of long duration, this considers an input of various frequencies, including higher frequencies up to 40Hz, of a rat whisker pad by electrical stimulation. As in the experimental data, there is a strong frequency dependence in the response amplitude of the model.

Figure 3.6 demonstrate the nonlinearity of the system with two examples. The inputs are the linear superposition of signals of different amplitudes or different frequencies and both the actual output and the linear superposition of the individual outputs are shown. The actual outputs are substantially smaller in amplitude than the linear superpositions of the individual outputs.

Much of the quantitative published data concerns the response at a single point, *i.e.*, a single pixel, to a stimulus at a single point, *e.g.*, a whisker pad stimulation. But

the model describes a 2 D array of pixels responding to a 2-D input signal. Figure 3.7 shows the 2-D response of the model as an image at various times in response to a single spatially-restricted stimulation and in response to a pair of spatially-restricted stimulations. The major point is the sublinear superposition of the responses to the pair of stimuli.

3.4 Grubb's Law

As was demonstrated in Section 2.3.3, the model can fit experimental data. However, it can also describe abstract relationships. To demonstrate this ability, in this section the model's predictions for Grubb's Law [6] relating cerebral blood volume and flow are presented.

Denote cerebral blood volume by *CBV* and cerebral blood flow by *CBF*. Grubb's Law [6, Eq. 5, p. 631] is the relationship

$$CBV / CBV_0 = 0.8(CBF / CBF_0)^{0.38} \tag{3.28}$$

where, in the units of Ref. [6, Eq. 5, p. 631] (*CBV* in milliliters of blood per 100gm and *CBF* in milliliters of blood per 100gm per minute), the constants CBV_0 and CBF_0 have numerical value 1.

The model described in this manuscript includes temporal and spatial dynamics which are not present in Grubb's Law. Therefore, to connect between the model and Grubb's Law it is assumed that the model is spatially homogeneous and in the steady state. Spatial homogeneity implies that the flows between pixels via T_l in Figure 2.2 are zero. Furthermore, Grubb's Law comes from imaging studies with voxels that are large compared to the length of a capillary so that, even in an inhomogeneous situation, the flow between pixels is small. Being in the steady state

implies that the capacitors are open circuit. Therefore the entire behavior of the model is determined by the serial connection of the five resistors $R^{(a)}$, $R(P_{i,j}^{(a)}(t),\delta_{E_{i,j}}(t))/2$, $R(P_{i,j}^{(a)}(t),\delta_{E_{i,j}}(t))/2$, $R(P_{i,j}^{(v)}(t),\delta_{E_{i,j}}(t))/2$, $R(P_{i,j}^{(v)}(t),\delta_{E_{i,j}}(t))/2$ between P_a and ground in the path T_0, T_a, and T_v of Figure 1(b) after the electrical circuits of Figure 2.5-6 are inserted into Figure 2.2. *CBF* is then the ratio of P_a divided by the sum of these five resistors. The voltages at the four nodes between the five resistors can all be computed by voltage divider calculations. Since now current flows through the resistors in T_l in Figure 1(b), it follows that $P_{i,j}^{(R)}(t)=P_{i,j}^{(0)}(t)$. From the voltages $P_{i,j}^{(R)}(t)$, $P_{i,j}^{(R)}(t)$, and $P_{i,j}^{(R)}(t)$, the charges $R(P_{i,j}^{(v)}(t),\delta_{E_{i,j}}(t))$, $R(P_{i,j}^{(v)}(t),\delta_{E_{i,j}}(t))$, and $R(P_{i,j}^{(v)}(t),\delta_{E_{i,j}}(t))$ can be computed and the sum of these charges is *CBV*. Since there is no time dependence, the "(*t*)" can be removed and since there is no special dependence the "*i,j*" can be removed.

Rather than using the circuit ideas of Section 2.2.3, outlined in the previous paragraph, to derive the equivalent of Grubb's Law for the model described in this manuscript, the underlying tube ideas of Section 2.2.1 and 2.2.2 are used. The contribution of $R(P_{i,j}^{(v)}(t),\delta_{E_{i,j}}(t))$, corresponding to arterioles is ignored since it is much smaller than the contribution from capillaries. The two contributions from capillaries, $R(P_{i,j}^{(v)}(t),\delta_{E_{i,j}}(t))$ and $R(P_{i,j}^{(v)}(t),\delta_{E_{i,j}}(t))$ are combined in terms of a total length l_c of capillaries. In the tube approach, if the length of the tube is l_c and the radius of the tube is a_c then

$$CBV = l_c \pi a_c^2. \tag{3.29}$$

Furthermore, if the pressure from end-to-end of the tube is P_c and the resistance to flow through the tube is R_c then

$$CBF = \frac{P_c}{R_c} = \frac{P_c}{8\eta l_c[\pi a_c^4]} = \frac{\pi P_c}{8\eta l_c} a_c^4 . \tag{3.30}$$

where the second equality is due to Poiseuille's formula (Eq 2.5). Solving Eq. 3.30 for a_c^2 and using the result in Eq. 3.29 gives

$$CBV = l_c \pi \sqrt{CBF \frac{8\eta l_c}{\pi P_c}} = l_c \sqrt{\frac{8\pi\eta l_c}{P_c}} CBF^{0.5} \tag{3.31}$$

which is the equivalent of Grubb's Law for the model described.

A more sophisticated resistance formula than Poiseuille's formula (Eq. 2.5) would alter the a_c^4 term in Eq. 3.30 which would alter the 0.5 exponent in Eq. 3.31. Therefore it may be possible to move the exponent closer to the value in Ref.[6, Eq. 5, p.631]. An alternate point of view is that viscosity η depends on radius a_c via a power law with unknown exponent, *i.e.*, $\eta = \eta_0 a_c^{2w}$ for some value of w [7,8], and use Grubb's law to estimate w. With this point of view, Eq. 3.30 becomes

$$CBF = \frac{P_c}{8\eta_0 a_c^{2w} l_c[\pi a_c^4]} = \frac{\pi P_c}{8\eta_0 l_c} a_c^{2(2-w)} \tag{3.32}$$

resulting in

$$a_c^2 = \left(CBF \frac{8\eta_0 l_c}{\pi P_c} \right)^{1/(2-w)} \tag{3.33}$$

which implies that

$$CBV = l_c \pi \left(CBF \frac{8\eta_0 l_c}{\pi P_c} \right)^{1/(2-w)} = l_c \pi \left(\frac{8\eta_0 l_c}{\pi P_c} \right)^{1/(2-w)} CBF^{1/(2-w)} . \tag{3.34}$$

In order to match the exponent value of 0.38 in Ref.[6, Eq. 5, p.631], it is necessary to have $1/(2-w) = 0.38$ which implies that $w = -0.63$.

P_c can be expressed in terms of P_a and the fundamental properties of tubes, specifically E_0, δ_E, a_0, t, and l, and the fundamental property of blood, specifically, η. First solve a 2-component vector fixed point equation constructed from two voltage divider formulas, specifically,

$$P^{(a)} = P_a \frac{R(P^{(a)}, \delta_E)/2 + R(P^{(v)}, \delta_E)}{R^{(a)} + R(P^{(a)}, \delta_E) + R(P^{(v)}, \delta_E)} \tag{3.35}$$

$$P^{(v)} = P_a \frac{R(P^{(v)}, \delta_E)/2}{R^{(a)} + R(P^{(a)}, \delta_E) + R(P^{(v)}, \delta_E)} \tag{3.36}$$

where $R(P,\delta_E)$ is defined bye Eq. 2.7 and the solution for $P^{(a)}$ and $P^{(v)}$ is denoted by $P_*^{(a)}$ and $P_*^{(v)}$, respectively. If the constant $R^{(a)}$ is also expressed in terms of the diameter of the arteriole by Poiseuille's formula then the constant η is not needed because it occurs in every resistance term and therefore cancels from the ratios. Then $P_c = 2P_*^{(v)}$. Using this value for P_c gives the constant for Eq. 3.31 in terms of system blood pressure P_a.

3.5 Discussion

This chapter presents a set of tools for modeling the cerebral microvasculature and demonstrates a complete model. Important goals that have been achieved are to describe both blood flow and cerebral blood volume, leading to use of both resistors and capacitors; to include the possibility that blood might enter the microvasculature in one pixel but exit from a different pixel; and to describe the flows and volumes of both oxygenated hemoglobin and deoxygenated hemoglobin and the conversion of

oxygenated into deoxygenated hemoglobin. Part of the model is closely based on physical principles, such as Kirchhoff's current and voltage laws, and Laplace's and Poiseuille's laws, while other parts are phenomenological, such as control laws. As demonstrated in Section 3.3, changing the parameters in the complete model described leads to quite different behaviors, *e.g.*, the presence or absence of an initial decrease in HbO_2 in response to an excitation. Finally, in Section 3.4, the model is connected to the macroscopic world by deriving Grubb's law.

The model built out of the components described above could be generalized in several ways. For instance, a voltage source (pressure source) is used to describe the heart. However, use of a current source would probably make it easier to describe blood "stealing" [11] where an area that is stimulated has increased flow and volume and surrounding areas have decreased flow and volume. Most general among linear models would be to use a Thévenin equivalent circuit for the heart, *i.e.*, a voltage source (pressure source) in series with a resistor.

Also related to blood "stealing" is the control law for the Young's modulus of the vessel walls. In Eqs. 20 and 21, Young's modulus is constrained to be between αE_0 and E_0 where E_0 is the resting value. Therefore, under no circumstances will the Young's modulus be greater than E_0, *i.e.*, in no cases will the vessel further constrict. This could be changed to introduce a resting Young's modulus E_{rest} such that $\alpha E_0 < E_{rest} < E_0$ in which case vessels could constrict relative to the resting state which would cause blood "stealing".

A major issue is the overall topology of the microvascular network. An increasing number of network topologies are becoming available from 2-photon laser

scanning microscopy (2PLSM) [3, 4]. A challenge is that they tend to fragment at depth, and so an estimation strategy that can determine a fully-connected network is a necessary and challenging part of using such networks in models of the type described above.

Linear systems are used to describe the phenomenological control laws. However, delays may provide more parsimonious descriptions. Delay-differential equations are usually not finite dimensional. However, if the equations are solved by a forward-Euler approach and all delays are an integral multiple of the step size in the I-Euler approach then it is still possible to solve the resulting equations in a straightforward manner.

Models constructed with these tools reproduce single-pixel OISI data from two different laboratories (Figures 3.4 and 3.5) and reproduce the sublinear superposition seen with multiple stimuli (Figure 3.7).

The methods described are really a toolbox for the construction of mathematical models rather than a single unique mathematical model. After having been validated on an initial set of experiments, such models can be used to predict the response to yet unperformed experiments. For example, predict the response of a mouse with polycythemia vera from the response of a normal mouse by changing just the blood dynamic viscosity parameter in Eq. 2.5 or predict the response of a mouse in an experiment done in a second laboratory with a second stimulus paradigm from the response of a mouse in the first laboratory with the first stimulus paradigm (by modification of Eq. 2.18) thereby aiding in the comparison of results between laboratories. The range of prediction is likely limited to situations with fundamentally

the same neurovascular physiology, *e.g.*, the response of a subject undergoing spreading depression or an epileptic seizure is probably poorly predicted by a model validated with normal data. Finally, models of this type may be useful ways to summarize intra-operative clinical data [12].

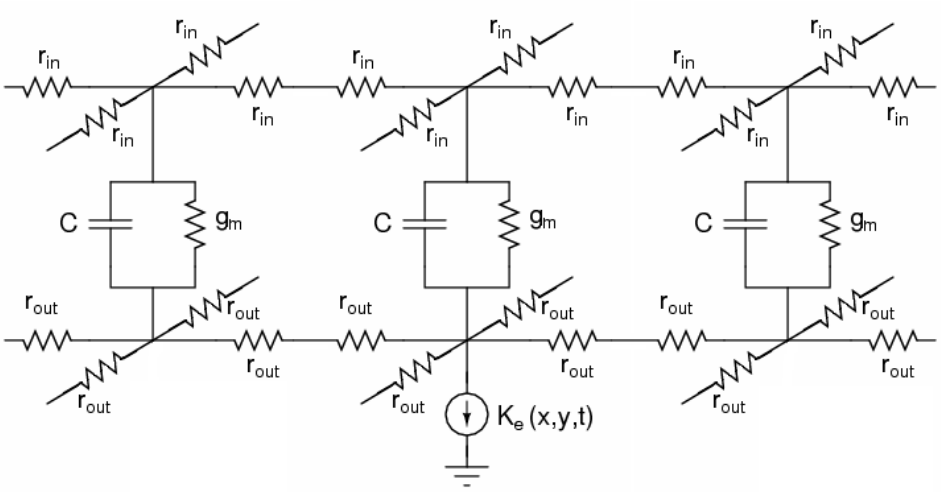

Figure 3.1: A diagram of the two-dimensional planar electrical layer circuit.

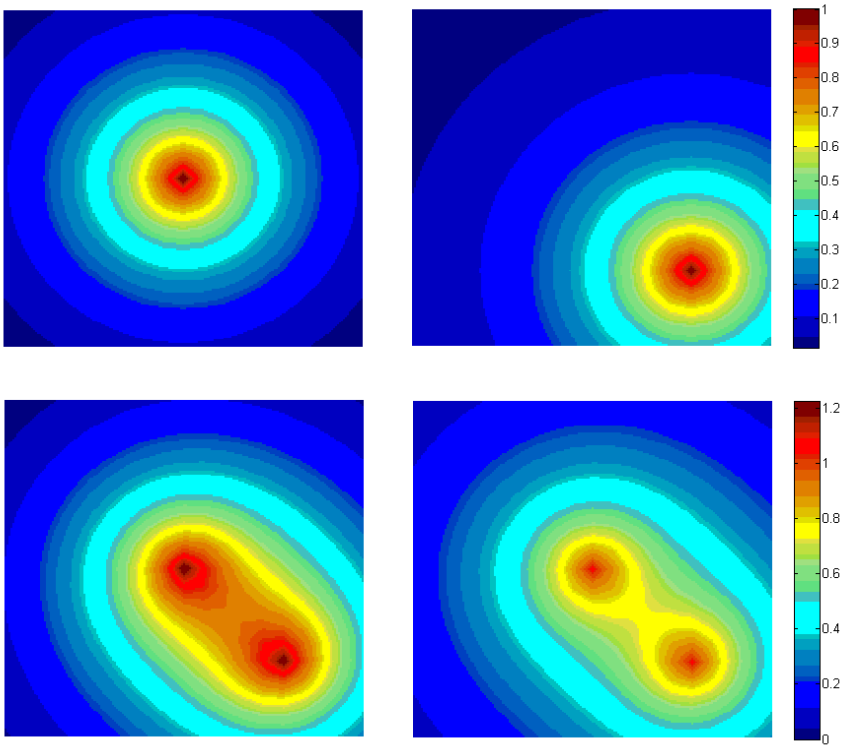

Figure 3.2: 2-D electrical layer output using the Sobolev norm-based model. The top two panels show individual normalized stimulation in two different areas of cortex. The bottom left panel shows linear superposition of the top two panels (*i.e.*, p=1). The bottom right panel shows the sublinear superposition of the top two panels with p=1.6. The same color map is used for the top two panels, and the same color map is used for the bottom two panels.

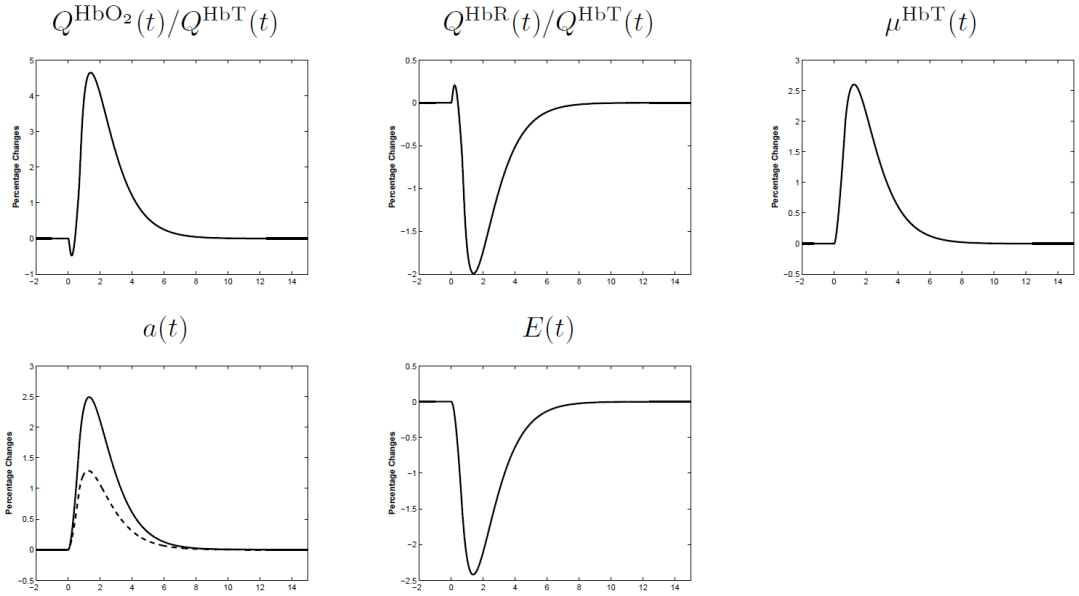

Figure 3.3: Behavior of the model with nominal parameters. Time course (units of seconds) of fractional changes in (1) concentration of oxygenated hemoglobin, (2) concentration of deoxygenated hemoglobin, (3) total mass of hemoglobin, (4) arteriolar diameter, and (5) Young's modulus. In the absence of the electrical layer, the input to the budget equation (Eq. 2.16) is directly controlled. The excitation (*p(t)* in Eq. (2.19) lasts 2s and is a sequence of positive-going pulses where the time interval between the leading edges of sequential pulses is 0.05s (*i.e.*, 20Hz).The budget (*e*(*t*)) starts at threshold and is driven below the threshold by the pulses, which results in dilation.

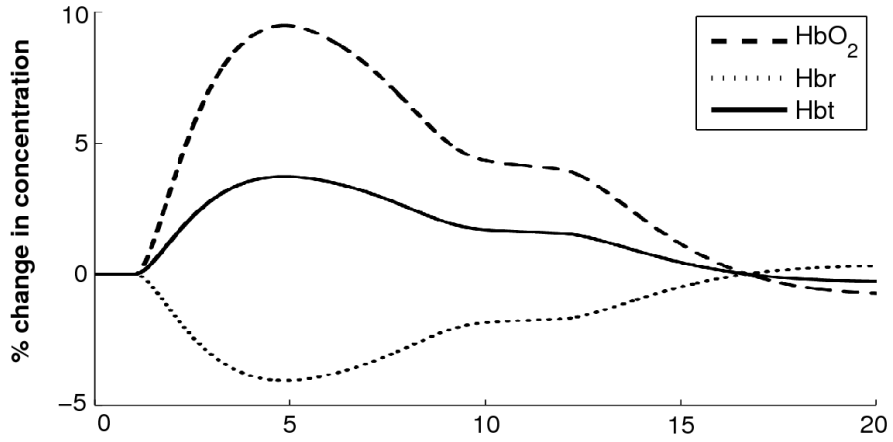

Figure 3.4 Simulated trajectories (time unit of seconds) of oxygenated, deoxygenated, and total hemoglobin concentrations (*Q* ratios) or masses (μ) in response to a 10s stimulation demonstrating a plateau midway through the response which is similar to experimental data from Ref. [9, Figure 3] which describes the response in a rat to forepaw stimulation at 3Hz for 10s. In the absence of the electrical layer, the input to the budget equation (Eq. 2.16) is directly controlled. The excitation (*p(t)* in Eq. (2.19) lasts 10s and is a sequence of positive-going pulses where the time interval between the

leading edges of sequential pulses is (1/3)s (*i.e.*, 20Hz).The budget ($e(t)$) starts at threshold and is driven below the threshold by the pulses, which results in dilation.

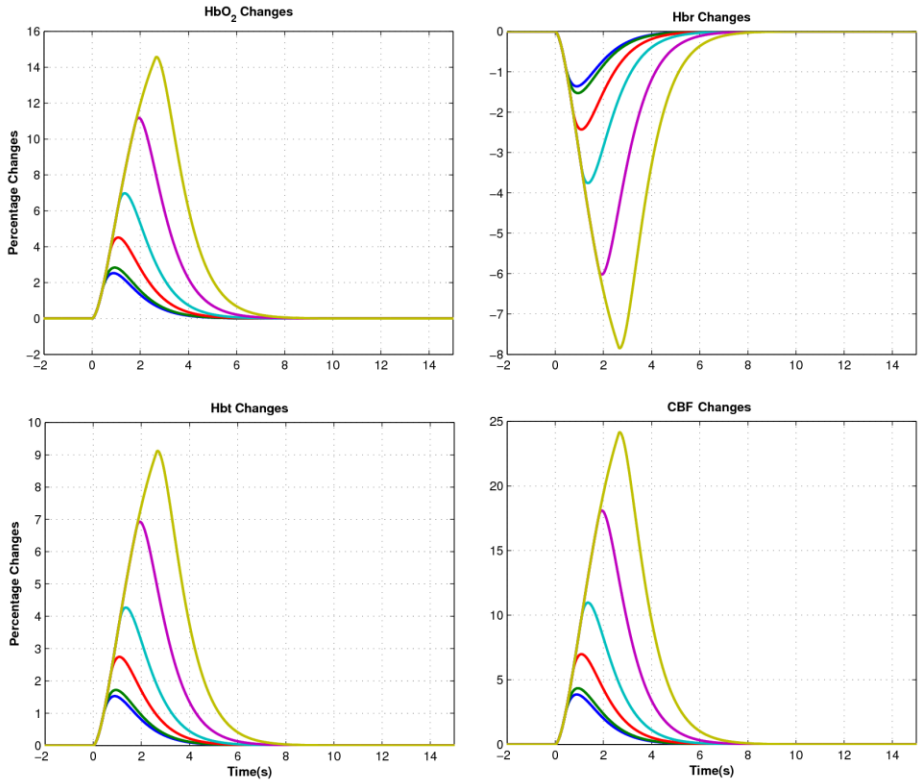

Figure 3.5 Simulated trajectories (time unit of seconds) of oxygenated, deoxygenated, and total hemoglobin concentrations (Q ratios) or masses (μ) in response to stimulations of varying frequencies which are similar to experimental data from Ref. [10, Figure 6] which describes the response in a rat to electrical stimulation of a whisker pad at 1-40Hz for 2s. In order of increasing amplitudes, the curves are for stimuli at 1, 2, 5, 10, 20, or 40Hz. In the absence of the electrical layer, the input to the budget equation (Eq. 2.16) is directly controlled. The excitation ($p(t)$ in Eq. 2.19) lasts 2s and is a sequence of positive-going pulses where the time interval between the leading edges of sequential pulses 1s, 0.5s, 0.2s, 0.1s, 0.05s, or 0.025s (*i.e.* 1, 2, 5, 10, 20, or 40Hz) in the six different curves. The budget ($e(t)$) starts at threshold and is driven below the threshold by the pulses, which results in dilation.

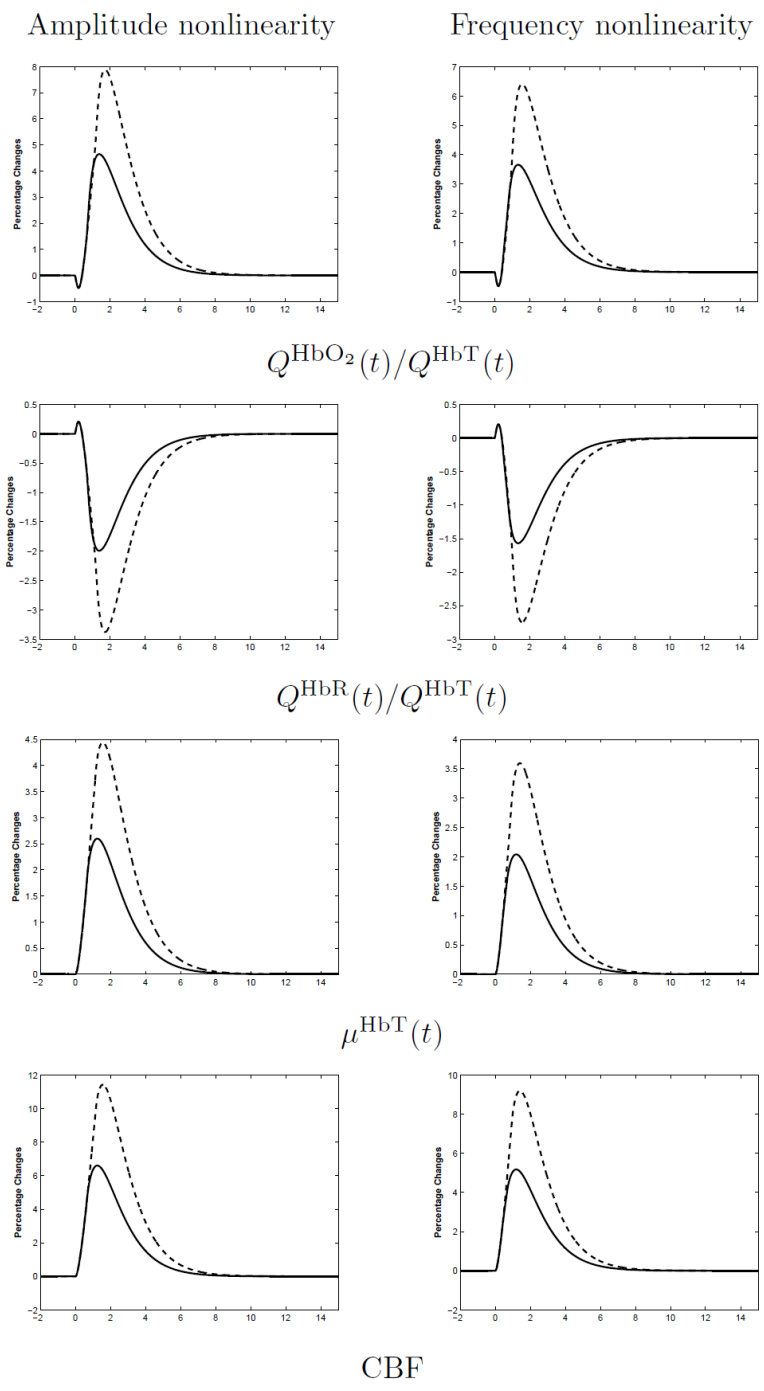

Figure 3.6: Nonlinearity with respect to amplitude and frequency of the excitation signals based on the model of Figure 3.3 with the excitations of Figure 3.5. The solid curves show the response of the system when excited by the sum of two excitations while the dotted curves show the sum of the responses to the individual excitations. The excitations for the amplitude example in the left column are both the 10Hz excitation from Figure 3.5 so the double excitation is the same as either single excitation with an amplitude scaled by a factor of 2. The excitations for the frequency example in the right column are the 10Hz and 20Hz excitations of Figure 3.5.

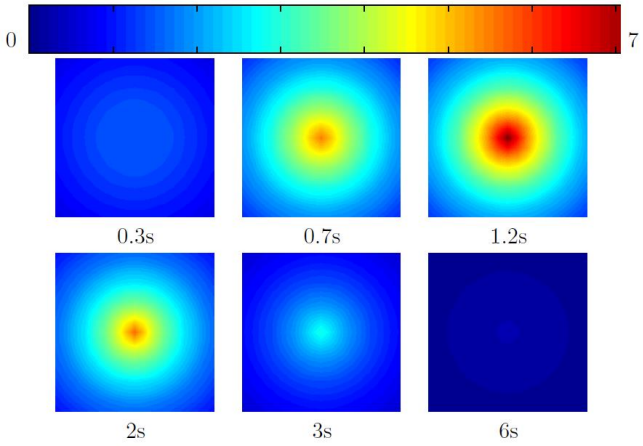

(a) One stimulus location.

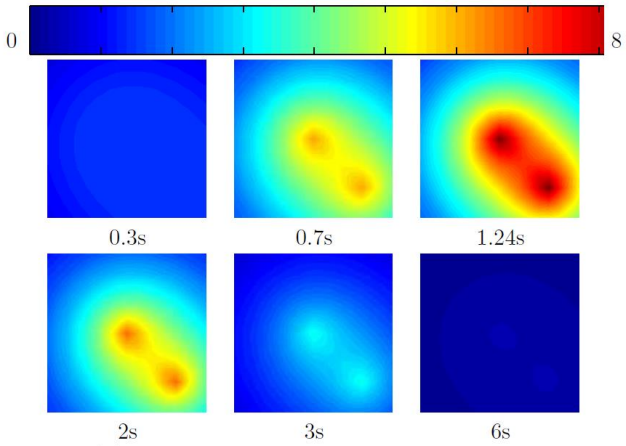

(b) Two stimulus locations of equal strength with linear superposition.

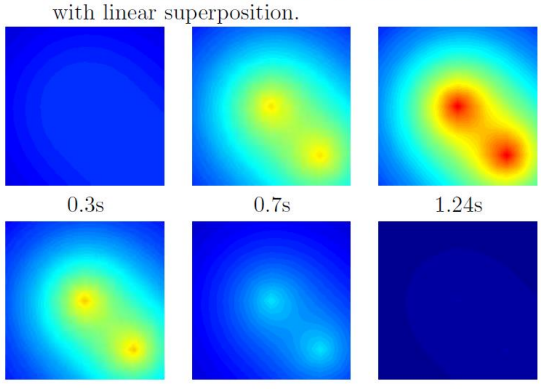

(c) Two stimulus locations of equal strength with sublinear superposition using the same colormap as Panel (b).

Figure 3.7: Images from the response of the 2-D model at the indicated times (units of seconds). The parameters are the nominal parameters of Figure 3.3. with the additional parameters (Eq. 3.1) of $c=\infty$, $z=4[\text{Pixel}]^{-1}$, and $p=1.6$ except for Panel I where $p=1$. The temporal characteristics of the input are unchanged from the input of Figure 3.3 and the pulse amplitude is 5. The same color map is used in all images of Panel (a) and in all images of Panel (b) and (c).

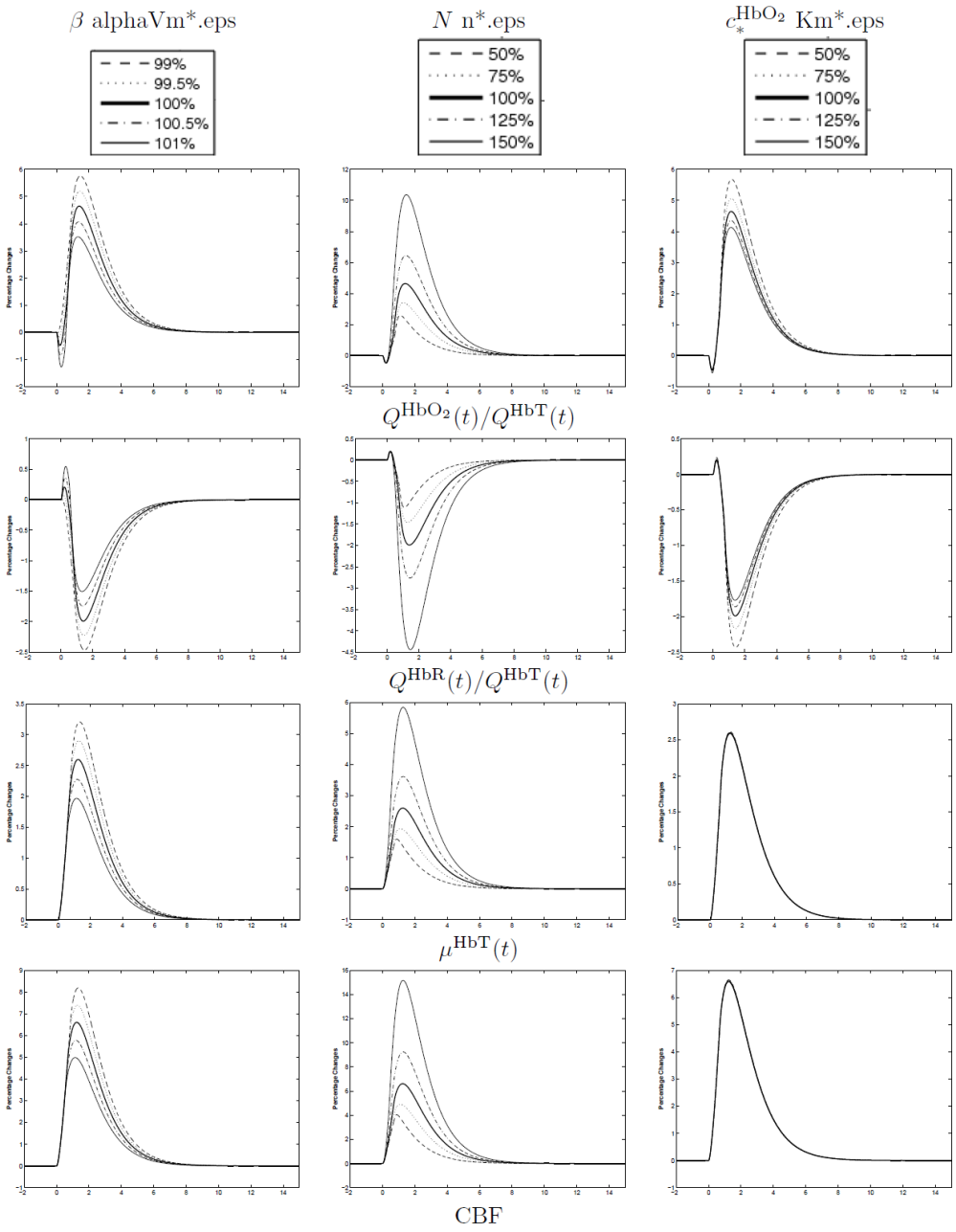

Figure 3.8: Sensitivity of the time course (units of seconds) of fractional changes in (1) concentration of oxygenated hemoglobin (Row 1), (2) concentration of deoxygenated hemoglobin (Row 2), (3) total mass of hemoglobin (Row 3), and (4) cerebral blood flow (Row 4) to changes in three of the parameters relative to the nominal values (Figure 3.3). The parameters that are perturbed are (1) the ratio between the two values of the maximum rate for the conversion of HbO_2 to HbR (Column 1), (2) the number of capillaries (Column 2), and (3) the half maximum rate for the conversion of HbO_2 to HbR (Column 3). The input is unchanged from the input of Figure 3.3. The curves in the second and third rows of the third column superimpose so accurately that only one curve is visible.

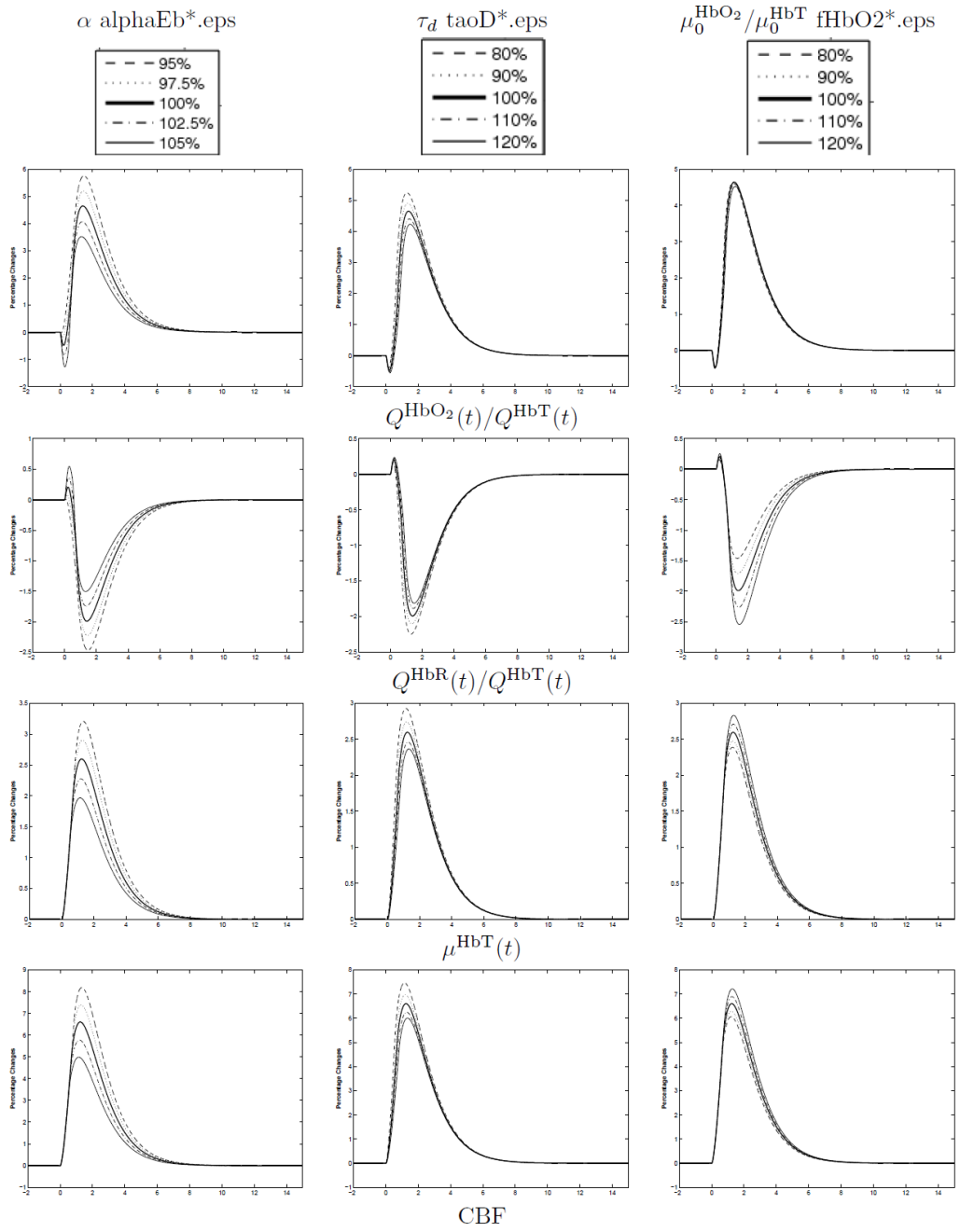

Figure 3.9: Sensitivity of the time course (units of seconds) of fractional changes in (1) concentration of oxygenated hemoglobin (Row 1), (2) concentration of deoxygenated hemoglobin (Row 2), (3) total mass of hemoglobin (Row 3), and (4) cerebral blood flow (Row 4) to changes in three of the parameters relative to the nominal values (Figure 3.3). The parameters that are perturbed are (1) the ratio of the steady state value of the Young's modulus in the dilated versus constricted states (Column 1), (2) the time constant for the decrease of the Young's modulus toward the dilated steady state (Column 2), and (3) the ratio of the baseline masses of HbO_2 to HbT (Column 3). The input is unchanged from the input of Figure 2.

REFERENCES

[1] Anna Devor, Peifang Tian, Nozomi Nishimura, Ivan C. Teng, Elizabeth M. C. Nillman, S. N. Narayanan, Istvan Ulbert, David A. Boas, David Kleinfeld, and Anders M. Dale. Suppressed neuronal activity and concurrent arteriolar vasoconstriction may explain negative blood oxygenation level-dependent signal. The J. of Neuroscience, 127(16):4452-4459, 18 Apr. 2007.

[2] Giovanni Mirabella, Stefano Battiston, and Matthew E. Diamond. Integration of Multiple-whisker Inputs in Rat Somatosensory Cortex. Cereb. Cortex, 11:164-170 Feb. 2001.

[3] Nozomi Nishimura, Nathanael L. Rosidi, Constantino Iadecola, and Chris B. Schaffer. Limitations of collateral flow after occlusion of a single cortical penetrating arteriole. J. Cerebral Bloof Flow & Metabolism, 30:1914–1927, 2010.

[4] Andy Y. Shih, Jonathan D. Driscoll, Patrick J. Drew, Nozomi Nishimura, Chris B. Schaffer, and David Kleinfeld. Two-photon microscopy as a tool to study blood flow and neurovascular coupling in the rodent brain. J. Cerebral Blood Flow & Metabolism, 32:1–33, 2012.

[5] Mathworks URL. www.mathworks.com/

[6] Robert L. Grubb, Jr., Marcus E. Raichle, John O. Eichling, and Michel M. Ter Pogossian. The effects of changes in PaCO2 cerebral blood volume, blood flow, and vascular mean transit time. Stroke, 5:630–639, 1974.

[7] A. R. Pries, T. W. Secomb, T. Gessner, M. B. Sperandio, J. F. Gross, and P. Gaehtgens. Resistance to blood flow in microvessels in vivo. Circulation Research, 75(5):904–915, November 1994.

[8] A. R. Pries and T. W. Secomb. Microvascular blood viscosity in vivo and the endothelial surface layer. Am. J. Physiol. Heart Circ. Physiol., 289:H2657–H2664, December 2005.

[9] Andrew K. Dunn, Anna Devor, Anders M. Dale, and David A. Boas. Spatial extent of oxygen metabolism and hemodynamic changes during function activation of the rat somatosensory cortex. NeuroImage, 27:279–290, 2005.

[10] Chris Martin, John Martindale, Jason Berwick, and John Mayhew. Investigating neural-hemodynamic coupling and the hemodynamic response function in the awake rat. NeuroImage, 32:33–48, 2006.

[11] Anna Devor, Istvan Ulbert, Andrew K. Dunn, Suresh N. Narayanan, Stephanie Jones, Mark L. Andermann, David A. Boas, and Anders M. Dale. Coupling of the cortical hemodynamic response to cortical and thalamic neuronal activity. Proc. Nat. Acad. Sci. U.S.A., 102(10):3822–3827, 8 March 2005.

[12] Minah Suh, Sonya Bahar, Ashesh D. Mehta, and Theodore H. Schwartz. Blood volume and hemoglobin oxygenation response following electrical stimulation of human cortex. NeuroImage, 31:66–75, 2006.

CHAPTER 4

ESTIMATING CORTICAL MICROVASCULAR BLOOD FLOWS FROM PARTIAL 2-PHOTON MICROCSOPY DATA BY COMPUTATION WITH A CIRCUIT MODEL

4.1 Introduction

The cortical microvasculature is comprised of a complicated network of arterioles, capillaries, and venules in which blood flow transports molecules to and from the cortical tissue. Since molecular transport across the blood-brain barrier primarily occurs in the microvasculature (especially in capillaries), these vessels are crucial to the metabolism, energetics, and functionality of the cortex. Occlusions, such as small stroke, are thus damaging to cortical health as they impede microcirculation.

Two photon laser scanning microscopy (2PLSM) allows *in vivo* imaging of the microvasculature to depths of 1mm, as well as blood flow measurements in vessels by tracking the time-varying position of individual red blood cells. While all vessels are within the microscope's imaging range (typically a $1mm^3$ volume) can be resolved, blood flow measurements can be made on only a subset of these vessels due to experimental limitations, such as the practical duration of anesthesia for a rat. The goal of the research is to use computational tools to estimate the blood flows in all the vessels. A model is thus needed to relate the measured and unmeasured blood flows. Inputs to the model are vessel diameter, length, interconnection topology, and the measured blood flows. The output of the model is predictions for flow velocity in every imaged vessel.

4.2 Methods and Materials

Methods for the two-photon microscopy data acquisition on anesthetized rats are described in [1]. The microvasculature is modeled as a resistive circuit in which current, q, is blood flow, and voltage, V, is blood pressure. Each vessel in the network represents a resistive branch that connects two nodes, or vessel bifurcation points, in the microvasculature. The circuit obeys Kirchhoff's current law (KCL), Kirchhoff's voltage law (KVL), and Ohm's law so that current is conserved at nodes and the voltage drop across a branch is proportional to the current through the branch and the branch's resistance. The resistance, R, of each branch is computed using Poiseuille's Law, assuming that the vessel is straight, which describes a relationship between length, l, radius, a, and blood viscosity, η, for nonturbulent flow. The formula is

$$R(l,\eta,a) = \frac{8\eta \mathrm{l}}{\pi a^4}. \tag{4.1}$$

In reality blood exhibits non-Newtonian flow characteristics because of its slurry-like composition of cells and plasma. To correct for non-Newtonian effects a diameter-dependent viscosity, $\eta(d)$, described by [2], [3] is used. As shown in Figure 6 of [2], the viscosity at hematocrit 45% varies by a factor of three over the range of vessel diameters greater than 10μm.

The microvasculature extends outside of the volume of brain that is imaged, as demonstrated in Figure 4.1 which shows a z-projection of 2PSLM topology data of surface vessels and penetrating arterioles. Therefore there are branches of the circuit that connect a node within the image to a node outside the image, and thus the circuit is incomplete. The circuit is completed by placing an unknown voltage source at each

cut branch. These voltages are referred to as boundary voltages. To the cut ends that are on the surface vessel side of the vascular system a voltage source of unknown value is attached whose other terminal is connected to ground. Voltage sources are used rather than a current source because the heart is more nearly a voltage source. To the cut ends that are on the capillary side of the vascular system, *i.e.*, to cut penetrating arterioles, each penetrating arteriole is lengthened by 1mm. Then, at the capillary end of the penetrating arterioles, a large common resistance of known value (representing the resistance of the capillary bed) is attached and connected to a ground.

Because of the many cut branches, the circuit has many input and many output nodes. Vessel bifurcations where vessels split or join are called internal nodes. Voltages at these nodes are called internal voltages. Figure 4.2 shows a small scale example of an imaged microvasculature topology and its corresponding circuit model. Figure 4.3 shows the region inside the rectangle in Figure 4.1, labeled with experimental flows and speeds and speeds.

Since the resistance values are known, once the voltage source values are known, the entire circuit is known and flows can be computed in any branch of the circuit. Therefore, the key computation is to estimate these voltage source values.

The mouse is anesthetized for multiple hours making it challenging to avoid alteration in its physiological state. Therefore it is assumed that the boundary voltages vary with time in the simplest possible manner, specifically, that the voltages vary linearly with time at a single rate common to all pressures. Therefore, for the *i*th pressure which is denoted by $V_i(t)$, the equation $V_i(t) = V_i^{(0)}(1+\varepsilon t)$ is used where t is time and $V_i^{(0)}$ and ε are constants.

For any set of values for the boundary pressures, the flows in any set of branches can be computed. Therefore the values of the boundary pressures can be determined by minimizing a weighted least squares criteria which measures the weighted squared distance between the optically-measured flows and the computed flows. The weight balances the importance of the flows in large and in small vessels (flows vary by more than 100 to 1) and the function $1/\log(1+\left|q_i^{measured}\right|)$ is used to weight the square of the difference between the optically-measured and the computed flows in the *i*th branch where $V_i^{(0)}$ is the optically-measured flow. The presence of both $V_i^{(0)}$ and ε means that the least squares problem is not linear. However, the problem is bi-linear, that is, if the value of ε is known then to determine the values of $V_i^{(0)}$ for all values of I is a linear vector weighted least squares problem while if the values of $V_i^{(0)}$ for all values of I are known, determining the value of ε is a linear scalar weighted least squares problem. This bi-linear problem is solved with an algorithm that takes advantage of the bi-linear structure. The algorithm is iterative and one iteration has two steps. First, for the current value of ε, compute a new set of values for $V_i^{(0)}$ for all values of I by the Moore-Penrose pseudoinverse which is computed in Matlab [4]. Second, using the values for $V_i^{(0)}$ from the first step as fixed, determine a new value for ε by the Moore-Penrose pseudoinverse. The algorithm iteratively progresses until convergence is achieved.

It is assumed that the times at which individual measurements are made are known exactly. If the flow in a particular vessel is measured multiple times, all measurements can be used in the weighted least squares problem if so desired.

The mathematics are described in the following paragraphs. Let I_n be the $n \times n$ identity matrix. Let N_{in} be the number of internal nodes and N_{bnd} be the number of boundary nodes. Let positive integers $I,j \in \{1,\ldots,N_{in}+N_{bnd}\}$ index the nodes. Let indexes $\{1,\ldots,N_{in}\}$ represent internal nodes, let indexes $\{N_{in}+1,\ldots, N_{in}+N_{bnd}-1\}$ represent boundary nodes where the boundary voltage sources are placed, and let index $N_{in} + N_{bnd}$ represent the ground node.

For simplicity in the equations, it is assumed that every pair of internal nodes is connected, with $R_{i,j}=R_{j,I}>0$. Currents between nodes are represented by $q_{i,j}$, where $q_{i,j}=-q_{j,i}$. Branches between nodes in the model that do not exist in the microvasculature will have resistance value of infinity. Thus current in these branches is zero, which in effect represents the absence of a connection between these nodes. Let the voltages at node I be denoted V_i. Define internal voltages, $V_{in}=(V_1,\ldots,V_{Nin})^T$, boundary voltages $V_{bnd}=(V_{Nin+1},\ldots,V_{Nin+Nbnd-1})^T$, and ground voltage $V_g=(V_{Nin+Nbnd})$. The vector containing both internal and boundary voltages (but not ground) is defined as $V=(V_{in}^T, V_{bnd}^T)^T$. The choice of the definition of ground has no effect on the results because the measurements are exclusively currents which depend solely on voltage differences.

At each of the N_{in} internal nodes, write KCL, *i.e.*, the sum of the currents entering (or leaving) the node is zero. For $n \in \{1,\ldots,N_{in}\}$, the form of the equations is

$$\sum_{m=1,m\neq n}^{N_{in}+N_{bnd}} \frac{V_n - V_m}{R_{n,m}} = 0 \tag{4.2}$$

which is equivalent to

$$V_n \sum_{m=1,m\neq n}^{N_{in}+N_{bnd}} \frac{1}{R_{n,m}} - \sum_{m=1,m\neq n}^{N_{in}+N_{bnd}} \frac{V_m}{R_{n,m}} = 0. \tag{4.3}$$

Subdivide the second sum to get

$$V_n \sum_{m=1,m\neq n}^{N_{in}+N_{bnd}} \frac{1}{R_{n,m}} - \left(\sum_{m=1,m\neq n}^{N_{in}} \frac{V_m}{R_{n,m}} + \sum_{m=N_{in}+1}^{N_{in}+N_{bnd}-1} \frac{V_m}{R_{n,m}} + \frac{V_{N_{in}+N_{bnd}}}{R_{n,N_{in}+N_{bnd}}} \right) = 0. \tag{4.4}$$

Use the fact that $V_{N_{in}+N_{bnd}} = 0$ since it is ground to get

$$V_n \sum_{m=1,m\neq n}^{N_{in}+N_{bnd}} \frac{1}{R_{n,m}} - \left(\sum_{m=1,m\neq n}^{N_{in}} \frac{V_m}{R_{n,m}} + \sum_{m=N_{in}+1}^{N_{in}+N_{bnd}-1} \frac{V_m}{R_{n,m}} \right) = 0. \tag{4.5}$$

Move terms that involve the boundary condition voltage sources to the right hand side of the equations to get

$$V_n \sum_{m=1,m\neq n}^{N_{in}+N_{bnd}} \frac{1}{R_{n,m}} - \sum_{m=1,m\neq n}^{N_{in}} \frac{V_m}{R_{n,m}} = \sum_{m=N_{in}+1}^{N_{in}+N_{bnd}-1} \frac{V_m}{R_{n,m}}. \tag{4.6}$$

Define two matrices of conductances, denoted by $G \in \Re^{N_{in}\times N_{in}}$ and $B \in \Re^{N_{in}\times(N_{bnd}-1)}$, by

$$G_{n,m} = \begin{cases} -\sum_{m=1,m\neq n}^{N_{in}+N_{bnd}} \frac{1}{R_{n,m}}, n = m \\ \frac{1}{R_{n,m}}, n \neq m \end{cases} \tag{4.7}$$

$$B_{n,m} = -\frac{1}{R_{n,m}}. \tag{4.8}$$

The negative of (4.7) can be written in the form

$$GV_{in} = BV_{bnd} \tag{4.9}$$

which implies

$$V_{in} = G^{-1}BV_{bnd}. \tag{4.10}$$

Finally,

$$V = \begin{bmatrix} V_{in} \\ V_{bnd} \end{bmatrix} = \begin{bmatrix} G^{-1}B \\ I_{N_{bnd}-1} \end{bmatrix} V_{bnd}. \tag{4.11}$$

All currents can be computed by

$$q_{i,j} = \frac{V_i - V_j}{R_{i,j}}. \tag{4.12}$$

Let $\alpha=(I,j)$, for $(I,j \in \xi=\{1,\ldots,N_{\text{in}}+N_{\text{bnd}}\})$, be an index describing a flow by giving the nodes at either end of the branch. Let $i=\varphi(\alpha)$ and $j=\psi(\alpha)$ be the node indices. Let $q^{(\xi)} = (q_{\phi(1),\psi(1)},\ldots,q_{\phi(N_\xi),\psi(N\varsigma)})$ be a vector whose elements are the flows.

Define $C \in \Re^{N_\xi \times N_{bnd}}$ with components $C_{\alpha,n}$ by

$$C_{\alpha,n} = \begin{cases} 1/R_{\phi(\alpha),\psi(\alpha)} & n = \phi(\alpha) \\ -1/R_{\phi(\alpha),\psi(\alpha)} & n = \psi(\alpha) \\ 0 & otherwise. \end{cases} \tag{4.13}$$

Then

$$q^{(\xi)} = CV = C\begin{bmatrix} G^{-1}B \\ I_{N_{bnd}-1} \end{bmatrix} V_{bnd} = L^\xi V_{bnd} \tag{4.14}$$

where $L \in \Re^{N_\xi \times N_{bnd}}$ is defined by

$$L^\xi = C\begin{bmatrix} G^{-1}B \\ I_{N_{bnd}-1} \end{bmatrix}. \tag{4.15}$$

Therefore, the predictor of the vector of currents, denoted by $q^{(\xi)}(V_{bnd})$, is

$$q^{(\xi)}(V_{bnd}) = L^\xi V_{bnd}. \tag{4.16}$$

Notice that it is perfectly reasonable to have the same current appear twice, in which case the corresponding two rows of C will be equal. Multiple appearances is the

way in which multiple measurements of the same current can be fit into the least squares problem.

As mentioned above, the experiment lasts 2-6 hours during which time there are both systematic and nonsystematic variations in the experimental subject's physiology. It is therefore necessary to account for at least the systematic variations. The systematic variations are conceived of as time-dependent boundary voltages. Three different types of time dependence are considered: (1) no dependence, (2) dependence of all voltages on time with the same proportionality constant, and (3) dependence of one subset of voltages on time with the complimentary subset of voltages independent of time. In this chapter, the subsets of boundary voltages that are considered in Case (3) are only surface arterioles versus penetrating arterioles. Cases (1) and (2) are subcases of Case (3) so in the remainder of this section, Case (3) is described.

Only affine dependence for the boundary voltages is considered so the *i*th boundary voltage, denoted by $(V_{bc})_i$ is described by

$$(V_{bnd}(t))_i = (V_{bnd}^{(0)})_i(1+\varepsilon t) \tag{4.17}$$

where ε is the same for all of the boundary voltages that are time dependent. Because the boundary voltages now depend on time, so do the predicted currents, specifically,

$$q^{(\xi)}(t) = L^{\xi}\begin{bmatrix} {}_0V_{bnd}(t) \\ {}_1V_{bnd} \end{bmatrix} \tag{4.18}$$

$$= \begin{bmatrix} {}_0L^{\xi} \vdots {}_1L^{\xi} \end{bmatrix}\begin{bmatrix} {}_0V_{bnd}(t) \\ {}_1V_{bnd} \end{bmatrix} \tag{4.19}$$

$$= \left[{}_0L^{\xi} \vdots {}_1L^{\xi} \right] \begin{bmatrix} {}_0V_{bnd}^{(0)}(1+\varepsilon t) \\ {}_1V_{bnd}^{(0)} \end{bmatrix} \tag{4.20}$$

$$= \left[(1+\varepsilon t)_0 L^{\xi} \vdots {}_1L^{\xi} \right] \begin{bmatrix} {}_0V_{bnd}^{(0)} \\ {}_1V_{bnd}^{(0)} \end{bmatrix} \tag{4.21}$$

where ${}_0V_{bnd}^{(0)}(t)$ are the boundary voltages that depend on time and ${}_1V_{bnd}^{(0)}(t)$ are the boundary voltages that are independent of time. In Eq. 4.21, all components of $q^{(\xi)}(t)$ are evaluated at the same time. However, in the experiment, different components are measured at different times. Therefore, the predictor for the experimental measurements is

$$q^{(\xi)}(t_1,\ldots,t_{N_\xi}) = \left[I_{N_\xi} + \varepsilon \mathrm{diag}((t_1,\ldots,t_{N_\xi}))_0 L^{\xi} \vdots {}_1L^{\xi} \right] \begin{bmatrix} {}_0V_{bnd}^{(0)} \\ {}_1V_{bnd}^{(0)} \end{bmatrix} \tag{4.22}$$

Therefore, the predictor of the vector of currents, denoted by $q_{\vec{t}}^{(\xi)}(\varepsilon, V_{bnd}^{(0)})$, is

$$q_{\vec{t}}^{(\xi)}(\varepsilon, V_{bnd}^{(0)}) = L_{\vec{t}}^{\xi}(\varepsilon) V_{bnd}^{(0)} \tag{4.23}$$

where $\vec{t} = t_1,\ldots,t_{N_\xi}$, and

$$L_{\vec{t}}^{\xi}(\varepsilon) = \left[I_{N_\xi} + \varepsilon \mathrm{diag}((t_1,\ldots,t_{N_\xi}))_0 L^{\xi} \vdots {}_1L^{\xi} \right] \tag{4.24}$$

The times $t_1,\ldots,t_{N_\xi}$ are known but neither ε nor $V_{bnd}^{(0)}$ are known. This is a nonlinear predictor equation because it involves products of ε and $V_{bnd}^{(0)}$.

A weighted least squares approach is used to predict the boundary voltages as a function of measured currents. Specifically,

$$\hat{\varepsilon}(\xi)\hat{V}_{bnd}(\xi) = \arg\min_{V_{bnd}} \left\| (q^{(measured,\xi)} - q_{\vec{t}}^{(\xi)}(\varepsilon, V_{bnd}^{(0)}))./\log(1+\left|q^{(measured,\xi)}\right|) \right\|_2^2 \tag{4.25}$$

where ./ indicates component-by-component division of one vector by another vector. If the problem is underdetermined, then there are many V_{bnd} that exactly achieve the global minimum described in Eq. 4.25. In this case, the particular V_{bnd} solution that has the minimum Euclidean norm is the one taken. In the case of predicting flows in the network shown in Figure 4.1, the problem is overdetermined because dimensionality is reduced drastically by connecting the arterioles to a common resistor which is connected to a ground.

4.3 Results

Computations were performed on the traced network depicted in Figure 4.1. Figure 4.3 shows an enlarged portion of the network inside the rectangle in Figure 4.1 with measured red blood cell speed measurements, diameter measurements, blood flow measurements extrapolated from a known flow profile, and measurement times.

In Figure 4.4, the flow in one of the vessels was measured at 14 different time points spread throughout the duration of a 2:20 hour experiment. Only the first of these time points is used in any of the estimates described in this chapter. Therefore, as shown in Figure 4.4, it is impressive that the time variation predicted by the model so accurately matches the additional 13 measurements, implying that a linear time dependence of boundary pressures is sufficient in the model.

The simplest validation is to test if the computation reproduces the measured results. For the sub-network imaged in the rectangle of Figure 4.1, such results are shown in Figure 4.5. Figure 4.6 shows a histogram of fractional error for all measured vessels compared to their corresponding flow predictions. For most vessels, error is between 0 and 1.

An important issue is how many and which flow measurements should be taken during the experiment so as to be able to compute an accurate estimate of the unmeasured flows. Suppose the voltage source values computed by this algorithm are correct. Then all flows can be computed. With a complete set of flows, it is possible to take subsets of the flows, solve a weighted least squares problem to estimate new voltage source values, use the new voltage source values to predict all flows, and compare this second set of predictions with the original set of computed values. Furthermore, the effect of Signal to Noise Ratio (SNR) can be studied because the values of the flows in the subset of flows can be degraded synthetically to arbitrary SNR before the weighted least squares problem is solved. Due to the large number of vessels in the network, there is an impractically large number of subsets with, for example, 30 vessels. Therefore, Monte Carlo calculations are performed where the number of vessels in the subset is constant but vessels in the subset are chosen at random. For each number of vessels in the subset 500 trials were included in the Monte Carlo calculation. The results of these calculations are shown in Figure 4.7. As expected, the higher noise levels in the synthetic measurements mean that the errors in the predictions grow faster as a function of the number of measurements that are deleted from the complete set of measurements.

A central motivation for studying the neurovascular system is to understand the cause and effect of strokes. In the models of this chapter, an embolic stroke in which one vessel is blocked can be described by setting the resistance of that vessel to infinity. If only one or a few vessels are blocked then it is natural to assume that the voltage source values do not change. Under these two assumptions (infinite resistance

in the involved vessel(s) and no change in voltage source values), it is straightforward to compute the flows in all branches of the circuit. The effect of the stroke on flows in other vessels can be described in a variety of ways.

Consider the case where only one vessel is blocked by a stroke. Figure 4.8 contains one example in which a penetrating arteriole is occluded and one example and a surface arteriole is occluded. In these particular examples, the effect of occluding a surface arteriole has a more widespread effect on the rest of the network.

The effect of a single occlusion on a non stroke vessel can also be categorized in terms of its topological location relative to the blocked vessel. Three positions are considered: n nodes downstream of the blockage, n nodes upstream of the blockage, or parallel to the blockage where a branch x is defined to be parallel to the blocked branch b if there is a parent branch p upstream to x such that both b and x are the same number of nodes downstream to p. Results are shown in Figure 4.9. The model results are qualitatively consistent with experimental findings. In particular, there are limited effects of an occluded arteriole on any surrounding vessels, however occluding a surface arteriole results in substantial flow decrease in nearby neighboring vessels along with a less noticeable change in flow in vessels farther away.

4.4 Discussion and Conclusions

A key component of this approach is the computation of the resistance of each vessel. Challenges include (1) no account is taken of the vessel tortuosity in computing the resistance because standard formulas do nut include such inputs (however, the vessel length is accounted for), and (2) experimental validation of the resistance formulas for vessels less than 10μm in diameter is not extensive [3]. If

improved resistance values become available, incorporating the improved values into the computations described in this chapter is straightforward.

Kirchhoff's Current and Voltage laws are used in order to write equations for the circuit and, therefore, the predicted flows exactly satisfy these laws. However, the experimental flow measurements violate Kirchhoff's Current Law. This could be due to several phenomena, including measurement errors and changes in the physiology of the animal during the experiment. By tracking physiology data on the animal during the experiment and developing regression models based on repeated flow measurements of the same branch, it was possible to decrease the effect of changes in physiology on the results.

Some measurements are much more important than others in terms of achieving accurate prediction of flows throughout the network, and in future work the hope is to characterize relative importance based on the topology of the network and the diameter of vessels in the network. Because error in a Monte Carlo run typically increases monotonically with number of omitted measurements, the higher variability in error in the central and right portions of the graph in Figure 4.7 means that certain sequences of omitted measurements can result in low error for a large number of vessel omissions, while other sequences result in high error very early on. This is important for the design of experiments, since measuring certain vessels is crucial to accurately estimating the behavior of the rest of the network. The tradeoff between number of measurements and accuracy of the measurements may be useful in guiding measurement development work.

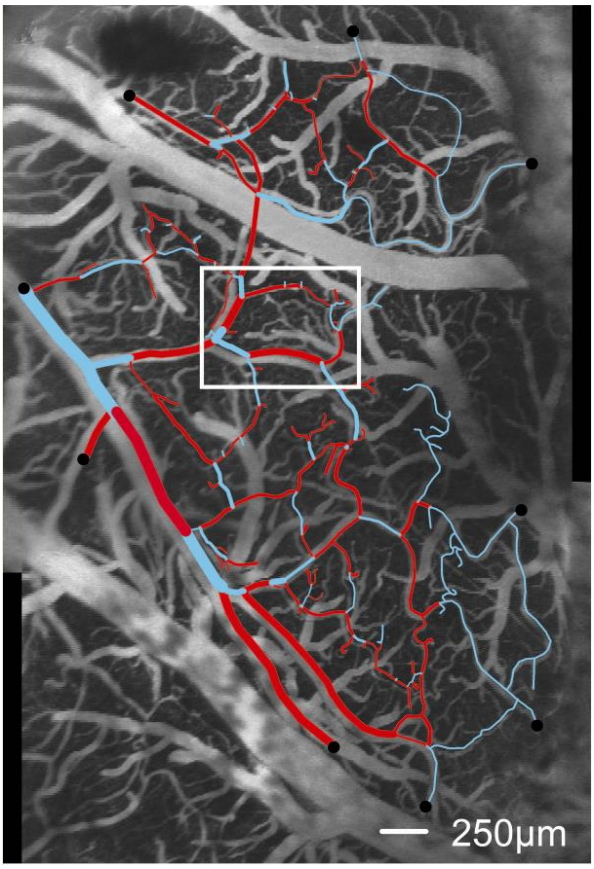

Figure 4.2: Z-projection of data from 2PEF. The traced vessels in color depict the entirety of the network. Vessel topology (lengths and diameters) is known for the entire network. Experimentally measured flow information is known for vessels in red. No flow information is known for vessels in blue.

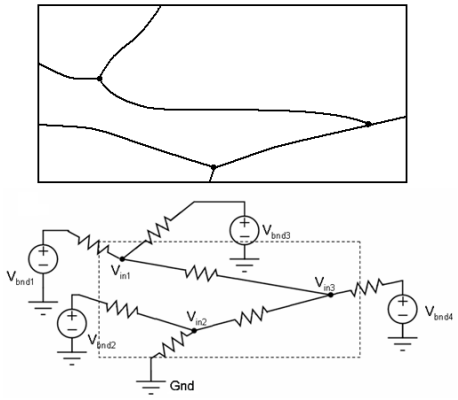

Figure 4.1: A small-scale example of a vessel topology with three internal nodes and five cut branches, and the corresponding circuit model shown below with voltage sources attached to the cut branches.

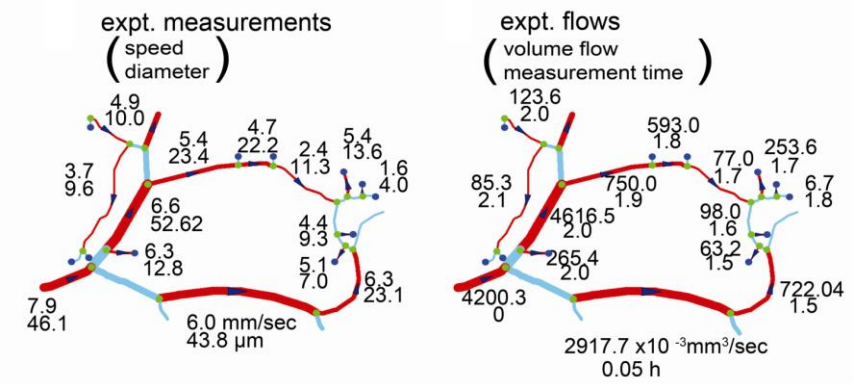

Figure 4.3: The region in the white rectangle from Figure 4.2 is enlarged and shown with experimentally measured red blood cell speeds and vessel diameters in the left panel, and extrapolated experimental flows and measurement times in the right panel. Arrows indicate the direction of flow. Red colored vessels correspond to vessels in which experimental flow speed measurements are known, and blue colored vessels correspond to vessels in which flow speeds are not known. The thickness of the line is proportional to the vessel's diameter.

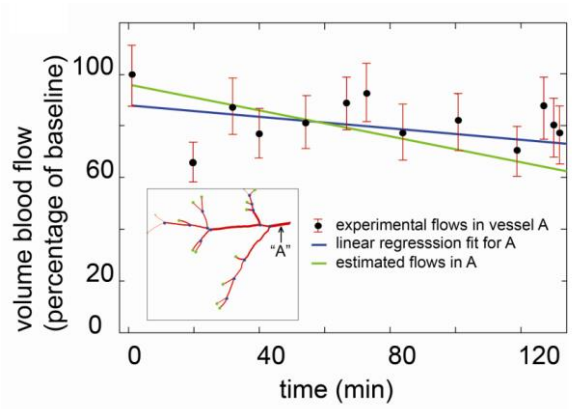

Figure 4.4: Linear dependence of flows on time determined by taking 13 measurements at the same location over the course of a 2:20 hour experiment.

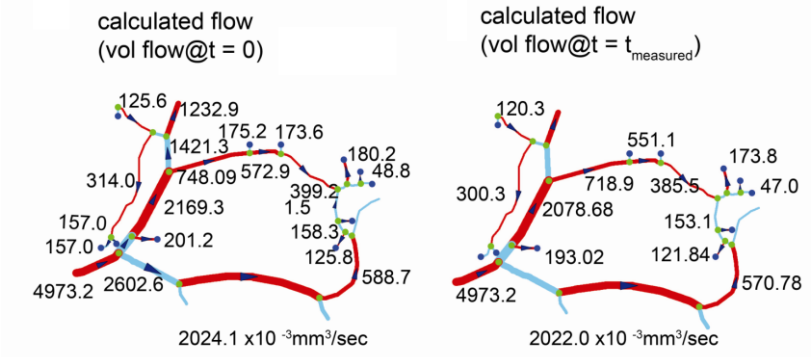

Figure 4.5: Topology and predicted flows from the model. The left panel shows predicted flows adjusted to t=0 in the experiment, and the right panel shows predicted flows at the time they were measured. Arrows indicate the direction of flow.

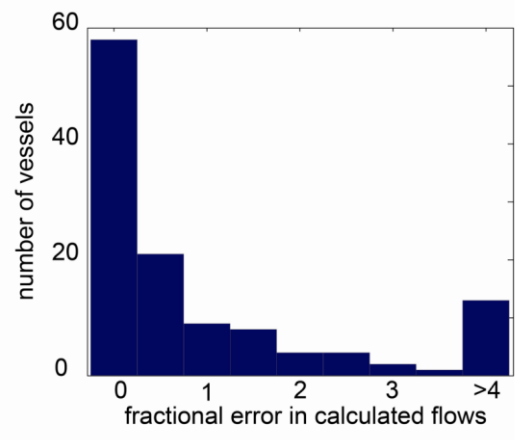

Figure 4.6: Histogram of fractional errors in the predicted flows compared to measured flows.

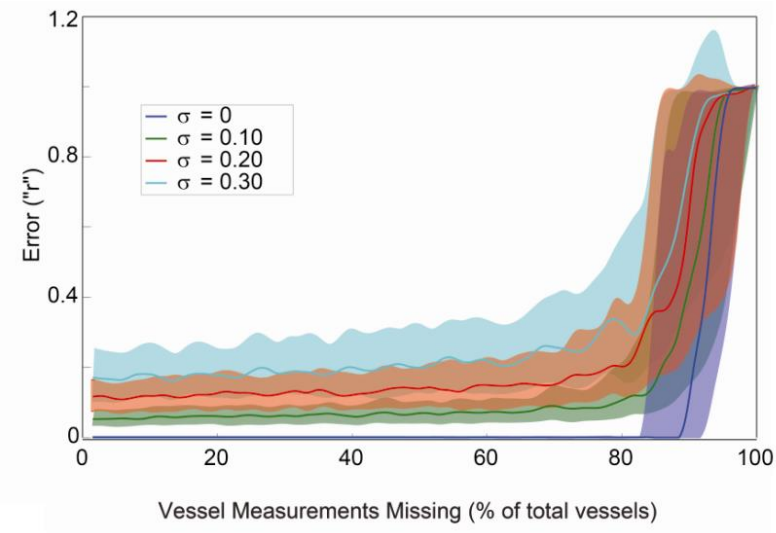

Figure 4.7: Error as a function of total number of vessel measurements missing..

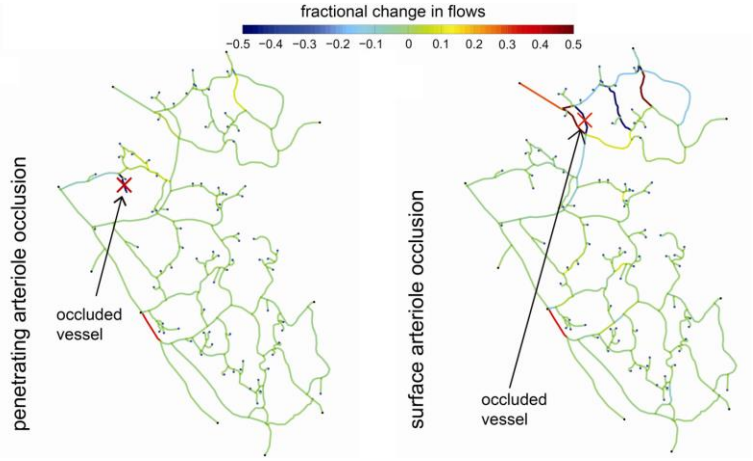

Figure 4.8: Effects of occlusions on flows. The left panel shows an occlusion to a penetrating arteriole, and the right panel shows an occlusion to a surface arteriole.

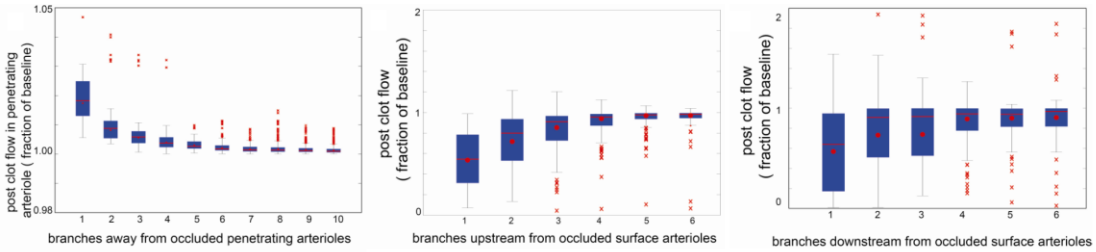

Figure 4.9: Box plots of fractional changes in blood flow from a simulated occlusion as a function of branches away from the occlusion. The left panel shows data for the number of branches away from an occluded penetrating arteriole, the middle for the number of branches upstream from an occluded surface arteriole, and the right panel for the number of branches downstream from an occluded surface arteriole.

REFERENCES

[1] N. Nishimura, N. Rosidi, C Iadecola, and C Schaffer, "Limitations of collateral flow after an occlusion of a single cortical penetrating arteriole," *J. Cereb Blood Flow Metab*, vol. 30, pp. 1914-1927, September 2010.

[2] A. Pries, T. Secomb, T. Gessner, M. Sperandio, J. Gross, and P. Gaehtgens, "Resistance to blood flow in microvessels in vivo," *Circ Res*, vol. 75, pp. 904-915, August 1994.

[3] A. Pries, T. Secomb, "Microvascular blood viscosity in vivo and the endothelial surface layer," *Am J Physiol Heart Circ Physiol*, vol. 289, pp. H2657-H2664, July 2005.

[4] Mathworks URL. www.mathworks.com/.

CHAPTER 5

RANDOM NETWORKS AND THEIR APPLICATION TO THE CORTICAL MICROVACULATURE

5.1 Introduction

The goal of this chapter is to present generative models of the cerebral vasculature rather than a set of statistics which might be sensitive to changes in the vasculature between two different types of subjects, *e.g.*, wild-type versus Alzheimer's susceptible mice.

A graph is a set of nodes N and edges E between nodes. A random graph is a probabilistic law for E. The phrase "random networks" will be used to mean a random graph plus geometry, meaning that the location of nodes in the graph and the existence of an edge between two nodes in the graph are based on random functions.

In order to model the cerebral vasculature, there are constraints on the random graph even before the geometry is added. For instance, since bifurcations of vessels are binary, it is necessary for nodes to be of degree three. In particular nodes of degree one (dead end branches of the vasculature) are forbidden.

Once geometry is added, there are still more constraints to address. For instance, the length of a branch is bounded above and below due to physiological limitations. In addition, the direction of a capillary vessel is roughly within a layer of the cortex so roughly horizontal. Arterioles and venules behave differently in that arterioles "dive" into the cortex while venules "ascend" out. Therefore constraints must also be placed on the maximum angle these vessels are allowed to deviate from perpendicularity to the cortical surface.

Constraints might be applied as hard constraints or soft constraints.

Three goals are defined for developing models that represent the cortical microvasculature.

1. Define stochastic generative models.
2. Develop statistical estimators for the parameters in the model from data.
3. Develop tests of differences, *i.e.*, are the parameters from one dataset significantly different from the parameters from a second dataset.

This chapter mainly concerns the first step.

Applications using these random network models can be developed within individual datasets as well. For example, as demonstrated in Section 5.5, it may be possible to predict cortical layer boundaries in mouse cortex using parameter estimation techniques based on the models.

5.2 Spatial Poisson Process Approach

This section defines a model that is constructed based loosely on the Erdős-Rényi model [1]. Consider a volume of cortex (denoted by V) with a surface (the true cortical surface, not the surface created by cutting V out of the entire brain) S. A microvasculature model can be created according to the following algorithm:

1. Create sites on S of penetrating arterioles: let the sites be located at the arrivals of a homogenous 2-D spatial Poisson process with rate λ_A.
2. The penetrating arterioles flow approximately straight and approximately normal to S and have many branches. Let the sites of branches be the arrivals of a homogenous 1-D Poisson process with rate λ_a.
3. Describe ascending venules in a similar manner but with rates λ_V and λ_v. (In some species, it has been experimentally shown that the number of ascending venules is somewhat larger than the number of penetrating arterioles so that $\lambda_V > \lambda_A$.)

4. Let branch points in the cortical parenchyma *V* be located at the arrivals of a homogenous 3-D spatial Poisson process with rate λ_c.
5. Connect the branch points (the nodes of the graph) by vessels (the edges of the graph) by making independent decisions at each pair of branch points in the spirit of Ref. [2]. However, the decisions are not identically distributed, *i.e.*, independent but not i.i.d. The reason for not i.i.d. is that branches should have appropriate length, neither too long nor too short, and appropriate direction, tending to stay within one cortical layer, or equivalently, to flow roughly parallel to the surface *S*.

   Let $\bar{x} \in V$. Let $\bar{x}_1$ and $\bar{x}_2$ be the locations of the two branch points. Let $\bar{\delta}_{1,2} = \bar{x}_1 - \bar{x}_2$ and $\delta_{1,2} = \left\| \bar{\delta}_{1,2} \right\|$. For each $\bar{x} \in V$, let $\hat{n}(\bar{x})$ be the local normal to the cortical surface *S* which is also the local normal to the layered structure of the cortex. Let $\bar{\eta}_{1,2} = (\hat{n}(\bar{x}_1) + \hat{n}(\bar{x}_2)) / \left\| \hat{n}(\bar{x}_1) + \hat{n}(\bar{x}_2) \right\|$. In simple situations, these definitions are straightforward. Suppose that *V* is small enough such that its surface is planar. Using a rectangular coordinate system such that $\hat{x}$ and $\hat{y}$ are the coordinates in the plane and $\hat{z}$ is the coordinate normal to the plane. Then $\hat{n}(\bar{x}) = \hat{z}$ for all $\bar{x}$ and therefore $\bar{\eta} = \hat{z}$ always.

   For any two vectors $\bar{x}$ and $\bar{y}$, the dot product is $\bar{x} \cdot \bar{y} = \left\| \bar{x} \right\| \left\| \bar{x} \right\| \cos(\theta)$ where θ is the angle between $\bar{x}$ and $\bar{y}$. Therefore, $\theta = \arccos(\bar{x} \cdot \bar{y} / \left\| \bar{x} \right\| \left\| \bar{y} \right\|)$ which is unique on [0, π]. Therefore the angle between $\bar{\eta}_{1,2}$ and $\bar{\delta}_{1,2}$ is $\theta_{1,2} = \arccos(\bar{\delta}_{1,2} \cdot \hat{\eta}_{1,2} / \left\| \bar{\delta}_{1,2} \right\|)$ since $\bar{\eta}_{1,2}$ is a unit vector. Continuing with the simple situation of the previous paragraph, $\theta_{1,2} = \arccos(\bar{\delta}_{1,2} \cdot \hat{z} / \left\| \bar{\delta}_{1,2} \right\|)$.

   Let the probability that an edge occurs between branch points $\bar{x}_1$ and $\bar{x}_2$ be denoted by $p_0(\bar{\delta})$ have value

$$p_0(\bar{\delta}_{1,2}; d_1, d_2, \psi) = \begin{cases} f_m(\delta_{1,2}) f_a(\theta_{1,2}), & d_1 \le \delta_{1,2} \le d_2 \quad \textit{and} \\ & \pi/2 - \psi \le \theta_{1,2} \le \pi/2 + \psi \\ 0, & \textit{otherwise} \end{cases} \qquad \text{Eq. 5.1}$$

$$p_0(\bar{\delta}_{1,2}; d_1, d_2, \psi, p_*) = \begin{cases} p_*, & d_1 \le \delta_{1,2} \le d_2 \quad \text{and} \\ & \pi/2 - \psi \le \theta_{1,2} \le \pi/2 + \psi \\ 0, & \text{otherwise} \end{cases}$$

The simplest situation is when $f_m()$ and $f_z()$ are constant. In that case

Eq. 5.2

In the simplest situation, the model has the following parameters: λ_A, λ_a, λ_V, λ_v, λ_c, d_1, d_2, ψ, and p_*.

Figure 5.1 shows an example of a model created using the above approach in a 100x100μm cube. Values for the parameters are: λ_A=5, λ_a=10, λ_V=5, λ_v=10, λ_c=150, d_1=10μm, d_2=30μm, ψ =π/6, and p_* =0.5.

Figure 5.2 shows a histogram of the number of edges connected to individual nodes. It is clear form the histogram that many of the nodes contain a number of edges that violate empirical observations of the microvasculature. In particular, nodes with degree one (dead ends) should not exist. Likewise nodes with degree greater than three should not exist. It is possible to enforce decision rules to ensure that each node has degree of either 0 (nodes floating in space which can be ignored), 2 (passing nodes), or 3 (bifurcation points), but many of these decision rules result in nodes that are no longer independent from one another. For example, enforcing a nearest neighbor rule in which an edge is established between a given node and its three nearest nodes in terms of Euclidean distance (resulting in a node with degree three) creates a dependence on the order in which the nodes are chosen. Establishing rules for edge deletion to pare down the network and enforce node degrees of 0, 2, or 3 result in similar dependency issues on order.

The distributions of the edge lengths, $\delta_{1,2}$, and edge angles, $\theta_{1,2}$, from the same example of Figure 5.1 are shown in Figure 5.3.

5.6 Spatial Poisson Approach with Different Parameters and a Deletion Rule

The statistics of networks generated using the Poisson process model outlined above can differ vastly based on the parameters selected for the model. For example, consider a network *N* that, for simplicity, contains only capillaries (*i.e.*, λ_V and λ_A are both 0). Now assume this network has a very high capillary node rate, λ_c, but a very low probability of an edge occurring between nodes, (*i.e.* small p_*). For a network of *N* nodes, the expected number of edges at each node is $(N-1)p_*$. If p_* is chosen small enough, the number of nodes with degree greater than 3 will probabilistically be very low, so that most nodes will have degree of either 0 (lone nodes which can be ignored), 1 (dead ends), 2 (passing nodes), or 3 (bifurcation points).

The existence of nodes with degree of one remains problematic. However, it is possible to sequentially delete these nodes and their corresponding edges until nodes of degree 1 no longer exist. Furthermore, the sequence in which these nodes and edges are deleted has no dependence on order.

An example of such a network prior to the deletion of degree 1 nodes is demonstrated in Figure 5.4. Values for the parameters are: λ_c=1000, d_1=10μm, d_2=30μm, $\psi = \pi/6$, and p_*=0.05. This particular network has 1003 nodes and 923 edges. The same network, with degree 1 nodes clipped off is shown in Figure 5.5. This network has been pared down to 365 nodes and 518 edges. Figure 5.6 shows a histogram of nodes with their degree number of the network in Figure 5.5. Nodes with degree 0 are ignored and not present in the histogram.

Deriving a formula to estimate number of nodes of a certain degree in a networks with sequentially deleted nodes of degree 1 is mathematically challenging. Therefore Monte Carlo simulations can be useful to gather statistics on the behavior of

these types of networks. Figure 5.6 shows a plot of the ratio of the number of nodes of degree 3 (bifurcation nodes) to the number of nodes of degree 4 or greater (physiologically unrealistic nodes) as a function of the probability that an edge occurs between two nodes. As the probability increases, the ratio moves towards zero since many nodes are of high degree compared to relatively few nodes of degree three, indicating that a low edge probability gives a more realistic model of a vascular network. Values for the parameters are: λ_c=1000, d_1=10μm, d_2=30μm, $\psi = \pi/6$, and p_* varies from 0.05 to 0.5. Each data point was taken from the mean of 25 Monte Carlo simulations with that particular probability.

5.5 Predicting Cortical Layer Boundaries

The Poisson approach to modeling a random network can be used in a variety of applications. Datasets can be analyzed based on the many different parameters of the model. For example, it may be possible to examine datasets based on the distribution of capillary lengths. Capillary lengths may be empirically observed to behave according to a particular distribution, such as a gamma or exponential distribution, whose parameters can be established using estimation techniques. Or perhaps capillary lengths can be assumed to be a member of one of two or more classes of Gaussians, and each class and membership can be determined by estimating the parameters of the Gaussian mixture.

Other model parameters such as node rates can also be of interest. In this section, a method of predicting cortical layer boundaries based on node rates within one vascular network dataset is proposed. Assume each layer of cortex is a striation parallel to the cortical surface and assume that nodes in each layer are Poisson distributed according to a node rate unique to that layer. Assume that z=0 at the cortical surface and z increases with depth into the cortex, and Z is the maximum depth. Proceed according to the following maximum likelihood estimation algorithm.

1. Select a number, N, of layer boundaries to estimate, (b_1, b_2,…,b_i,…,b_N), where b_i is a positive scalar in the z-direction and $0<b_1,<b_2<\ldots<b_i<\ldots<b_N<Z$.
2. Choose a discretezation step for the z-direction, Δz, large enough that it contains several nodes, but small enough to maintain adequate spatial resolution in the z-direction.
3. Compute the Poisson likelihood (or log-likelihood) function, for every combination of boundaries at each discrete step in the z-direction, maintaining that $0<b_1<b_2<\ldots<b_i<\ldots<b_N<Z$.
4. The set of layer boundaries where the maximum of these likelihood function values occurs corresponds to the optimal cortical layer boundary choices.

An example of one such dataset in which three cortical layers (two layer boundaries) are predicted is shown in Figure 5.7. This particular dataset contains 814 nodes in a cube imaged to a depth of 255μm.

5.6 Markov Random Field Approach

The idea is to create a field in which space is discretized and, at each location in space, have a random variable that is either a 0 (no vessel present) or 1 (vessel present). With a sufficiently small discretization step, a broad range of vessels and trajectories can be described.

A binary bifurcations requirement is included as a soft constraint. A restriction on dead end vessels is also included as a soft constraint. Difficulties arise in introducing rules to enforce upper and lower bounds on branch lengths. Directionality constraints can possibly be included by favoring horizontal over vertical branches. The algorithm used to construct the field is discussed in the following paragraphs.

Let μ be the dimension of the problem, which is likely to be 2 or 3. Let $\bar{\nu} \in Z_+^\mu$ be the size of the lattice. Let

$$N = \{0,...,\nu_1 - 1\} \times ... \times \{0,...,\nu_\mu - 1\} \tag{5.3}$$

be the lattice. Let $\bar{n} \in N$ be an index into the lattice. Let

$$\phi : N \to \{0,1\} \tag{5.4}$$

be the binary lattice variables where "unoccupied" and "occupied" are equivalent to taking value 0 and 1, respectively.

Let N_n be the sites that are neighbors of the site $\bar{n}$, defined by

$$N = \begin{cases} \{\bar{n} + (1,0)^T, \bar{n} - (1,0)^T \bar{n} + (0,1)^T \bar{n} - (0,1)^T\}, \mu = 2 \\ \{\bar{n} + (1,0,0)^T, \bar{n} - (1,0,0)^T \\ \bar{n} + (0,1,0)^T, \bar{n} - (0,1,0)^T \\ \bar{n} + (0,0,1)^T, \bar{n} - (0,0,1)^T\}, \qquad \mu = 3 \end{cases} \tag{5.4}$$

except at the boundary of the lattice where adjustments are needed in order to impose free or toroidal boundary conditions. Let $\eta(\bar{n}, \phi)$ be the number of neighbors of site $\bar{n}$ in the lattice that are occupied, *i.e.*,

$$\eta(\bar{n}, \phi) = \sum_{\bar{n}' \in N} \phi(\bar{n}') \tag{5.5}$$

$$= \begin{cases} \phi(\bar{n} + (1,0)^T) + \phi(\bar{n} - (1,0)^T) + \phi(\bar{n} + (0,1)^T) + \phi(\bar{n} - (0,1)^T), \ \mu = 2 \\ \quad \phi(\bar{n} + (1,0,0)^T) + \phi(\bar{n} - (1,0,0)^T) \\ \quad + \phi(\bar{n} + (0,1,0)^T) + \phi(\bar{n} - (0,1,0)^T) \\ \quad + \phi(\bar{n} + (0,0,1)^T) + \phi(, \bar{n} - (0,0,1)^T), \qquad \mu = 3 \end{cases} . \tag{5.6}$$

Note that the range of $\eta(\cdot,\cdot)$ is limited to $\{0,1,...,\eta_*\}$ where

$$\eta_* = \begin{cases} 4, & \mu = 2 \\ 6, & \mu = 3 \end{cases} . \tag{5.7}$$

The Hamiltonian has several parts. Generally, terms are included twice since if $\bar{n}'$ is a neighbor of $\bar{n}$ there is one contribution from $\bar{n}$ and a second from $\bar{n}'$.

1. A sufficient number of occupied sites is desired. Therefore,

$$H_1(\phi) = -\sum_{\bar{n}\in N} \alpha_1 \phi(\bar{n}) \tag{5.8}$$

where α_1>0. Alternatively, there might be a target value, denoted by ρ, for the density of the vascular system (*e.g.*, μ length per μ^3 volume). In this case,

$$H_1'(\phi) = -\alpha_1' \left(\rho - \sum_{\bar{n}\in N} \phi(\bar{n}) \right)^2 \tag{5.9}$$

where $\alpha_1 > 0'$. H_1' seems undesirable since it connects all sites in the lattice.

2. A sufficient number of nodes is desired in the random graph. A node is to be defined as an occupied site which has three or more occupied neighbor sites. Therefore,

$$H2(\phi) = -\sum_{\bar{n}\in N} \alpha_2 \phi(\bar{n}) \delta_{\eta(\bar{n},\phi),3} \tag{5.10}$$

where α_2>0.

3. Nodes of order three, representing vessel bifurcations, are of particular interest. Therefore, occupied sites should have either two occupied neighbors (in which case it is not a node in the bifurcation sense), or three occupied neighbors (in which case it is a node in the bifurcation sense). Define the Kronecker delta function $\delta_{i,j} : Z \times Z \to \{0,1\}$ by

$$\delta_{i,j} = \begin{cases} 1, & i = j \\ 0, & i \neq j \end{cases}. \tag{5.11}$$

Therefore,

$$H_3(\phi) = -\sum_{\bar{n} \in N} \alpha_3 \phi(\bar{n})(\delta_{\eta(\bar{n},\phi),2} + \delta_{\eta(\bar{n},\phi),3}) \tag{5.12}$$

where $\alpha_2 > 0$.

4. Consider just $\mu=3$. Define

$$\nu(\bar{n},\phi) = \phi(\bar{n} + (0,0,1)^T) + \phi(\bar{n} - (0,0,1)^T) \tag{5.13}$$

which is the number of occupied neighbor sites above or below. Note that $\nu(\cdot,\cdot) \in \{0,1,2\}$. Mostly horizontally-directed branches are desired.

Therefore

$$H_4(\phi) = -\sum_{\bar{n} \in N} \phi(\bar{n}) \varepsilon(\nu(\bar{n},\phi)) \tag{5.14}$$

where the function $\varepsilon(\cdot,\cdot)$ is really only three numbers since the range space of $\nu(\cdot,\cdot)$ is limited. An interplay exists between the level of "rewarding" $v=0$ versus "penalizing" $v=1,2$.

A fairly general Hamiltonian might be

$$H(\phi) = -\sum_{\bar{n} \in N} \left[\alpha \phi(\bar{n}) + \phi(\bar{n}) \gamma(\nu(\bar{n},\phi)) + \phi(\bar{n}) \varepsilon(\nu(\bar{n},\phi)) \right]$$

$$= -\sum_{\bar{n} \in N} \phi(\bar{n}) \left[\alpha + \gamma(\nu(\bar{n},\phi)) + \varepsilon(\nu(\bar{n},\phi)) \right]$$

$$= -\alpha \sum_{\bar{n} \in N} \phi(\bar{n}) - \gamma(0) \sum_{\bar{n} \in N} \phi(\bar{n}) \delta_{\eta(\bar{n},\phi),0} - \gamma(1) \sum_{\bar{n} \in N} \phi(\bar{n}) \delta_{\eta(\bar{n},\phi),1} - \ldots - \gamma(\eta_*) \sum_{\bar{n} \in N} \phi(\bar{n}) \delta_{\eta(\bar{n},\phi),\eta_*} \tag{5.15}$$

where the function γ is really just $\eta_* + 1$ numbers because the range of $\eta(\cdot,\cdot)$ is just $\{0,1,\ldots,\eta_*\}$.

In preparation for approximations, it is common to write the Hamiltonian as a polynomial even though the lattice variables are binary. Suppose that j is fixed. In order to write $\delta_{i,j}$ as a polynomial of minimal order in i, it is necessary to know the range of i. In the previous expressions, $i = \eta(\bar{n}, \phi) \in \{0,1,..., \eta_*\}$. An expression for $\delta_{i,j}$ that is polynomial in i is

$$\delta_{i,j} = \frac{\prod_{k=0,k\neq j}^{\eta_*}(i-k)}{\prod_{k=0,k\neq j}^{\eta_*}(j-k)}. \tag{5.16}$$

For μ=2 this specializes to

$$\delta_{i,j} = \frac{i(i-1)...(i-(j-1))(i-(j+1))...(i-4)}{j(j-1)...(j-(j-1))(j-(j+1))...(j-4)} \tag{5.17}$$

which specializes to

$$\delta_{i,0} = \frac{(i-1)(i-2)(i-3)(i-4)}{(-1)(-2)(-3)(-4)} \tag{5.18}$$

$$= \frac{(i-1)(i-2)(i-3)(i-4)}{24} \tag{5.19}$$

$$\delta_{i,1} = \frac{(i)(i-2)(i-3)(i-4)}{(1)(-1)(-2)(-3)} \tag{5.20}$$

$$= \frac{(i)(i-2)(i-3)(i-4)}{6} \tag{5.21}$$

$$\delta_{i,2} = \frac{(i)(i-1)(i-3)(i-4)}{(2)(1)(-1)(-2)} \tag{5.22}$$

$$= \frac{(i)(i-1)(i-3)(i-4)}{4} \tag{5.23}$$

$$\delta_{i,3} = \frac{(i)(i-1)(i-2)(i-4)}{(3)(2)(1)(-1)} \tag{5.24}$$

$$= \frac{(i)(i-1)(i-2)(i-4)}{6} \tag{5.25}$$

$$\delta_{i,4} = \frac{(i)(i-1)(i-2)(i-3)}{(4)(3)(2)(1)} \tag{5.26}$$

$$= \frac{(i)(i-1)(i-2)(i-3)}{24} \tag{5.27}$$

To achieve expressions, such as $\delta_{i,2+}\ \delta_{i,3}$, it is possible to add the polynomials for the two delta functions to get a new polynomial of (typically) the same order.

An example of a two-dimensional Gibbsian Markov Random Field model is shown in Figure 5.8. The example shows a network that is clearly physiologically unrealistic. Firstly, connectivity in Figure 5.8 is too low to represent a network of vessels. The network shown is a collection of many vessel "islands" that are separate from each other. Secondly, as in the Poisson process model described in Section 5.2, dead end vessels and nodes with degree greater than three still exist, despite being probabilistically unfavorable in the Hamiltonian. Gibbsian Markov Random Field models of this type are powerful in areas such as percolation theory, however additional ideas are required to more realistically represent vessel networks in the cortical microvasculature.

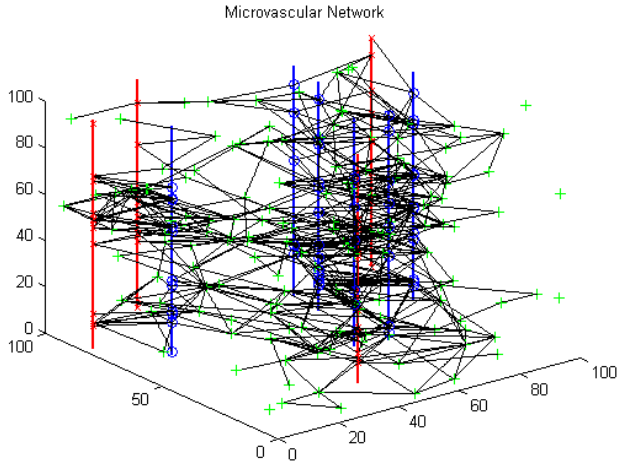

Figure 5.1: An example of a microvascular network computer using the Poisson model approach. Pictured are four ascending venules (red vertical lines), six diving arterioles (blue vertical lines), and 605 capillaries (black lines). Nodes sites on ascending venules are red x's, node sites on diving arterioles are blue x's, and capillary nodes are green +'s. In total there are 244 nodes.

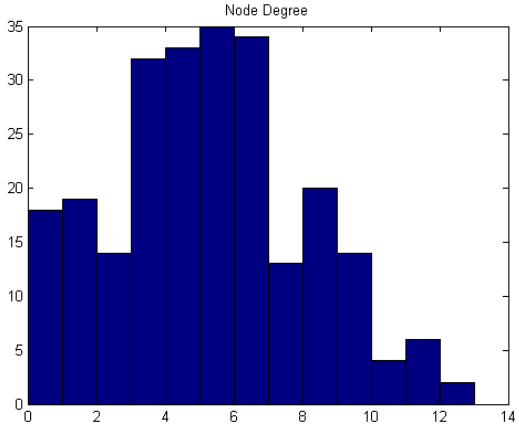

Figure 5.2: A histogram of nodes and their degree.

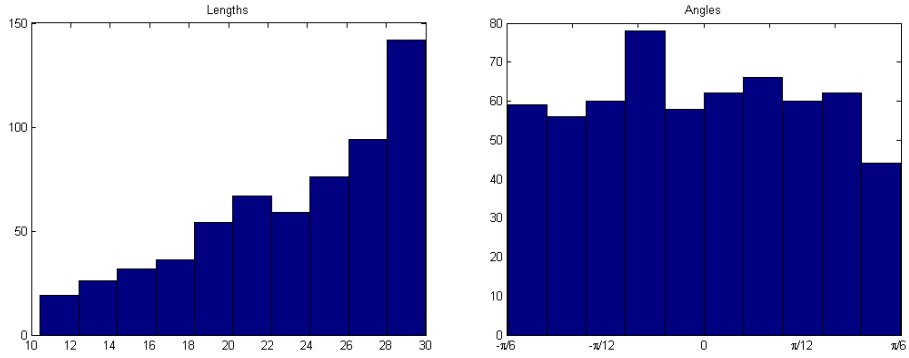

Figure 5.2: A histogram of capillary length (left) and capillary angle with respect to the cortical surface (right). In the model, parameters for d_1=10 μm, d_2=30 μm, and $\psi = \pi/6$.

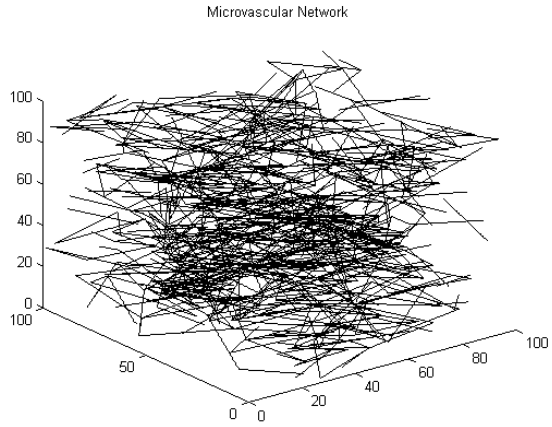

Figure 5.3: An example of a network with a high node rate, but low probability of edge success. This particular example is of only capillaries and has 1003 nodes and 923 edges.

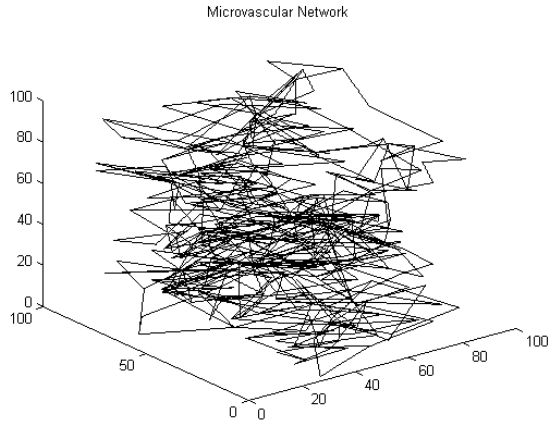

Figure 5.4: The same network as shown in Figure 5.3 except nodes with degree 0 are deleted, and nodes with degree 1 (and connecting edges) are sequentially deleted until only nodes of degree 2 or more remain. In this network, 365 nodes and 518 edges remain.

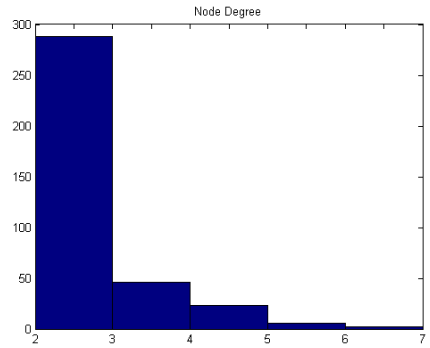

Figure 5.5: A histogram of nodes and their degree number following sequential deletion of nodes with degree 0 or 1.

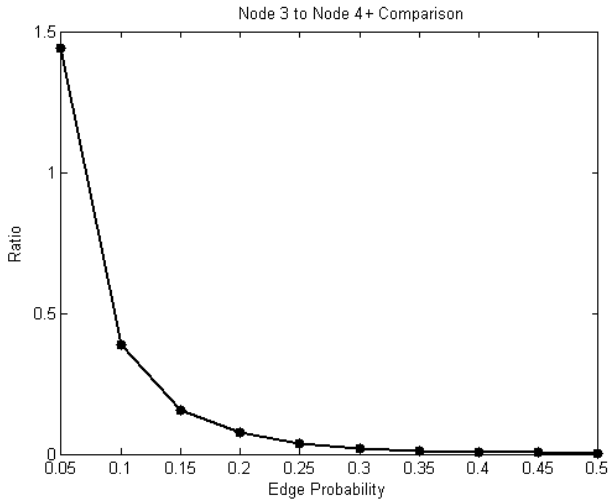

Figure 5.6: A plot of the ratio of the number of nodes with degree 3 to the number of nodes with degree 4 and greater as a function of edge probability. As the probability that an edge exists between two nodes is increased, the ratio goes towards zero because the number of nodes with degree 3 is relatively few compared to the number of nodes with degree 4 or greater.

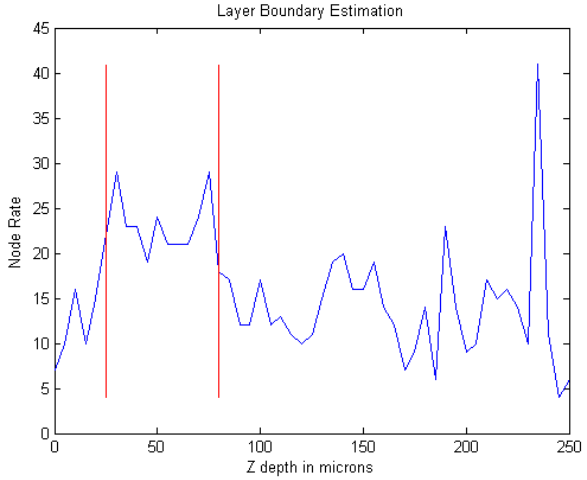

Figure 5.7: A plot of node rate as a function of z-depth in the cortex. The red horizontal lines represent locations where cortical layer boundaries are predicted to occur based on maximum likelihood estimators using node rates as a function of z-depth.

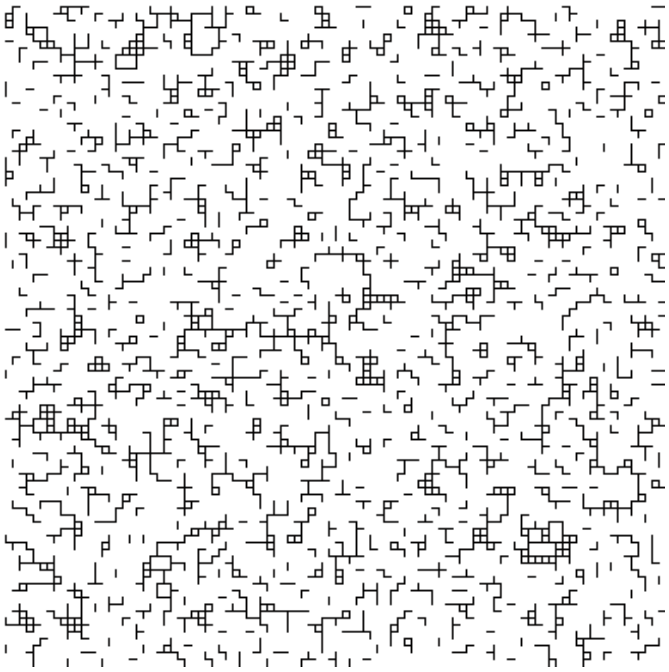

Figure 5.8: A sample network computed using a Gibbsian Markov Random Field approach.

REFERENCES

[1] Paul Erdős and Alfréd Rényi. On Random Graphs. Publ Math. pages 6:290-297, 1959

[2] E. N. Gilbert. Random graphs. Annals of Mathematical Statistics, 30(4):1141:1144, December 1959.

CHAPTER 6

CONCLUSION

As advancements in imaging and microscopy progress, higher quality data will be produced to further elucidate functionality of the brain. Currently, several modalities exist to image cortical function on multiple levels and multiple time scales. This work has proposed models which connect mainly to OISI and 2PSLM data, but it should be emphasized that these models are presented as simply a toolbox and can be extended to connect to data from modalities such as positron emission tomography (PET), laser spectral contrast imaging (LSCI), and fMRI.

The first model presented in Chapters 2 and 3 is a multi-compartment model constructed to achieve the goal of interpreting OISI data. Each compartment in the model contains a multitude of parameters, each of which can be manipulated to produce a unique output to reflect a high variability of blood flow, volume, and oxygenation level image data. The compartments are designed to be modular so that a particular set of ideas or physiological representations can be used, depending on information available regarding the physiological behavior of a particular compartment. For example, a Michaelis-Menten model is currently used in the metabolic layer, but this is just one choice of many pharmacokinetic models that can be used to describe metabolism. Furthermore, a feedback system for the energy budget is used in the current metabolic layer and vascular layer to create a dynamic interaction between the two layers, but feedforward ideas can instead be implemented to reflect data which may suggest that, for example, vessel dilation occurs as a feedfoward response to the presence of neurotransmitters (a proxy for neural activity) in the local tissue. The current model also uses a Sobolev norm-based electrical layer,

but other unique layers can be constructed to represent electrical activity in the cortex, such as the circuit model presented in Section 3.2.2.

Many challenges were present in developing the end-to-end model, one in particular being computational difficulties in solving many nonlinear ordinary differential equations in time and space. The simple approach to computing the model output is using a forward Euler method in which differential equations are solved at each time instant and each pixel. Limits are therefore imposed on temporal and spatial resolution based on computational power and memory. Furthermore, improper handling of the differential equations leads to machine error propagating into the output of the model. Possible development and/or implementation of more sophisticated ordinary differential equation solving techniques as well as increased computer processing power and memory could mitigate these difficulties, resulting in increased spatial resolution and reduced computation time.

The second model of this work, presented in Chapter 4, offers a framework for estimating time-varying blood flows in a network based on blood flow measurements from a subset of vessels in the network. One possible extension of this model would be to attach a Thévenin equivalent circuit to the cut branch of each surface arteriole. Similarly, a model could be proposed in which a unique unknown resistor is attached to each of the cut surface arteriole branches, and these unknown resistors are then attached to a common unknown voltage source. This model could be considered more physiologically realistic in that only one voltage source representing the heart is present, and the upstream resistance between each surface arteriole and the voltage source (heart) is accounted for. Both models increase in complexity compared to the current model because nonlinearities arise in estimating both voltages and resistances.

Chapter 5 outlines random graph models for neurovascular topology based on both a Poisson approach and a Gibbsian Markov Random Field approach. Future work

involving the Poisson approach can be especially useful in better understanding network topologies, partly due to the simplicity of the model as well as the simplicity of the network statistics. In Section 5.5 one application of this model is shown by its ability to predict cortical layer boundaries using maximum likelihood estimators. A multitude of other applications can be proposed based on the availability of certain types of data. One potentially useful investigation using this model would be comparing two different types of vascular network datasets. One types of dataset could, for example, be from mice predisposed to Alzheimer's disease, while the other could be from wild type mice. Statistics regarding node rates, capillary lengths, capillary angles, arteriole and venule densities, *etc*. could all be analyzed to determine if a meaningful difference exists between the two types of mice, possibly leading to a better understanding of the causes and/or effects of Alzheimer's.

For other future work, an obvious undertaking would be to merge parts of multiple models to create a more complete representation of blood flow and the hemodynamic response in the neural microvasculature. For example, the end-to-end model from Chapters 2 and 3 could contain a vascular layer which is constructed in a physiologically realistic way, rather than a geometrically simplified way, by introducing vessel network topologies from data used in the blood flow prediction model of Chapter 4. A diameter dependent viscosity is used in the model of Chapter 4, but not in the end-to-end model of Chapters 2 and 3 mainly because of mathematical difficulties arising from taking time derivatives of complicated diameter-dependent equations. A challenge in merging these models would be to find a mathematically tractable equation to represent time-varying diameter-dependent viscosity in diameters relevant to the data being modeled.